SAND REPORT
SAND2002-4055
Unlimited Release
Printed December 2002

Rapid ultrasensitive chemical-fingerprint detection of chemical and biochemical warfare agents.

Carol I.H. Ashby, Timothy J. Shepodd, W. Graham Yelton, and David J. Muron

Prepared by
Sandia National Laboratories
Albuquerque, New Mexico 87185 and Livermore, California 94550

Sandia is a multiprogram laboratory operated by Sandia Corporation, a Lockheed Martin Company, for the United States Department of Energy under Contract DE-AC04-94AL85000.

Issued by Sandia National Laboratories, operated for the United States Department of Energy by Sandia Corporation.

Available to DOE and DOE contractors from
U.S. Department of Energy
Office of Scientific and Technical Information
P.O. Box 62
Oak Ridge, TN 37831

Telephone: (865)576-8401
Facsimile: (865)576-5728
E-Mail: reports@adonis.osti.gov
Online ordering: http://www.doe.gov/bridge

Available to the public from
U.S. Department of Commerce
National Technical Information Service
5285 Port Royal Rd
Springfield, VA 22161

Telephone: (800)553-6847
Facsimile: (703)605-6900
E-Mail: orders@ntis.fedworld.gov
Online order: http://www.ntis.gov/help/ordermethods.asp?loc=7-4-0#online

SAND2002-4055
Unlimited Release
Printed June 2003

Rapid Ultrasensitive Chemical-fingerprint Detection of Chemical and Biochemical Warfare Agents

Carol I. H. Ashby
Microsensors Science and Technology

Timothy J. Shepodd
Materials Chemistry

W. Graham Yelton
Photonic Microsystems Technology

David J. Muron
Microsensors Science and Technology

Sandia National Laboratories
P.O. Box 5800
Albuquerque, New Mexico 87185-1425

Abstract

Vibrational spectra can serve as chemical fingerprints for positive identification of chemical and biological warfare molecules. The required speed and sensitivity might be achieved with surface-enhanced Raman spectroscopy (SERS) using nanotextured metal surfaces. Systematic and reproducible methods for preparing metallic surfaces that maximize sensitivity have not been previously developed. This work sought to develop methods for forming high-efficiency metallic nanostructures that can be integrated with either gas or liquid-phase chem-lab-on-a-chip separation columns to provide a highly sensitive, highly selective microanalytical system for detecting current and future chem/bio agents. In addition, improved protein microchromatographic systems have been made by the creation of acrylate-based porous polymer monoliths that can serve as protein preconcentrators to reduce the optical system sensitivity required to detect and identify a particular protein, such as a bacterial toxin.

Table of Contents

Page intentionally left blank.

Executive Summary

Unambiguous identification of chemicals and biochemicals usable as chem/ bio weapons (CBW) is essential at nanomolar levels with short analysis times (<5 min.) Vibrational spectra can serve as chemical fingerprints for positive identification of CBW molecules. The required speed and sensitivity might be achieved with surface-enhanced Raman spectroscopy (SERS) using nanotextured metal surfaces. Although ordinary SERS produces sensitivity enhancements on the order of 10^3 vs. normal Raman spectroscopy, a properly nanotextured metal surface can increase sensitivity up to 10^{14} - fold.

Systematic and reproducible methods for preparing stationary metallic surfaces that maximize sensitivity have not been previously developed. This LDRD program was to investigate the integration of chemical-fingerprint identification of CBW molecules using SERS as the detector in the chip-scale microseparation columns developed under the Sandia MicroChemLab program. To this end, this program was to develop methods for forming high-efficiency metallic nanostructures that could be integrated with either gas or liquid-phase chem-lab-on-a-chip separation columns to provide a highly sensitive, highly selective microanalytical system for detecting current and future chem/bio agents. In addition to speed and sensitivity, the chemical fingerprinting provided by SERS would enable rapid identification of new, non-standard CBW agents that might be introduced to avoid detection by established sensor systems.

Improved methods for on-chip separation of biomolecules, such as proteins, were a prerequisite for the application of SERS as a detector in microchromatograpic systems. Chromatographic separation media based on porous polymer monoliths were to be developed in this program to insure efficient separation and purification of proteins, such as biotoxins, prior to their detection and identification using SERS.

The goals of this LDRD were three-fold:

1) Development of a manufacturable surface that possessed a very high density of metallic nanostructures that enable highly efficient surface enhanced Raman spectroscopy (SERS) of a wide range of chemicals, especially those used as chemical and biological weapons.

2) Development of miniaturized chromatographic systems capable of separating the numerous proteins that might be encountered in an environmental sample. Special emphasis was to be placed on the chromatographic support media required to effect such separation on the microscale.

3) Integration of the highly efficient SERS metallic surfaces as part of spectroscopic detector systems for both liquid-phase microchromatographs and conventional gas-phase chromatographs. Integration of the SERS sensitization surface as a detector with the chromatographic media in a microchemlab architecture suitable for demonstrating a human-portable field instrument was planned.

Termination of funding of the originally 3-year program after two years prevented the accomplishment of the desired surface from Goal 1. Goal 2 was highly successful in achieving its goals and was preparing to increase its efficiency beyond that original envisioned when funding was terminated. Goal 3 was not attempted due to termination before accomplishing Goal 1.

Introduction

A real-world environmental sample may contain hundreds of different chemical compounds in a complex matrix. When one needs to identify the presence of a particular chemical in such a sample, it is usually necessary to isolate that compound from the original matrix to avoid interferences that can preclude successful identification. This is especially true when using a diagnostic technique that generates a very complex spectrum, such as vibrational spectroscopy. Since the intensity and energy associated with every vibration in a molecule is affected by the structure and bonding of every atom in the molecule, a virtual "chemical fingerprint" is displayed in the Raman vibrational spectrum of that molecule. Since there are 3N-6 normal vibrational modes for a nonlinear molecule of N atoms, the complexity of the spectrum from the chemicals of particular interest as chemical or biological weapons is great. This myriad of peaks in the vibrational spectrum that provides the fingerprint generally requires that a single chemical compound, or at the very least only a very few compounds, be present in the region being sampled by the spectroscopic system. The goals of this LDRD were three-fold:

1) Development of a manufacturable surface that possessed a very high density of metallic nanostructures that enable highly efficient surface enhanced Raman spectroscopy (SERS) of a wide range of chemicals, especially those used as chemical and biological weapons.

2) Development of miniaturized chromatographic systems capable of separating numerous proteins that might be encountered in an environmental sample. Special emphasis was to be placed on the chromatographic support media required to effect such separation on the microscale.

3) Integration of the highly efficient SERS metallic surfaces as part of spectroscopic detector systems for both liquid-phase microchromatographs and conventional gas-phase chromatographs. Integration of the SERS sensitization surface as a detector with the chromatographic media in a microchemlab architecture suitable for demonstrating a human-portable field instrument was planned.

Termination of funding of the originally 3-year program after two years prevented the accomplishment of the desired surface from Goal 1. Goal 2 was highly successful in achieving its goals and was preparing to increase its efficiency beyond that original envisioned when funding was terminated. Goal 3 was not attempted due to termination before accomplishing Goal 1. The following summarizes the progress made prior to termination of the program.

Metallic Nanostructures for Surface-Enhanced Raman Spectroscopy

The Raman process involves the inelastic scattering of incident light where the Raman-scattered light is shifted up or down in energy by an amount equal to a vibrational frequency of the molecule. The intensity of down-shifted light (Stokes shifted) is

generally much larger and is routinely measured in Raman spectroscopy. The intensity (I_{scat}) of the Stokes-shifted light depends on the number of molecules in the excitation volume (N), the intrinsic scattering cross-section for a particular vibration (σ_0), and the magnitude of the optical electric field (E) at the molecules.

$$I_{scat} \propto N \sigma_0 E^2$$

The effective cross-section, σ, is defined as $\sigma_0 E^2$. The SERS enhancement factor (EF) is defined as σ/σ_0.

The key to success in the SERS portion of the program hinges on the fabrication of nanotextured metallic surfaces that possess a high areal density of features that produce very large near-surface enhancements of the electric field of the impinging light, thereby producing large values of EF. Excitation of surface plasmons in the metal by the impinging light can lead to orders of magnitude increase in the electric field at and near the metallic surface. Typical SERS surfaces, such as electrochemically roughened Au or Ag, typically produce enhancements of 10^3 to 10^5 due to the relatively low areal density of regions with highly enhanced electric fields. To realize the goal of spectra with S/N greater than 20 in 1 sec using < 1 mW excitation power requires an EF on the order of 10^9. Fabrication of a surface capable of producing such an enhancement was the goal of this project.

Recent reports of single-molecule SERS for hemoglobin, DNA, and crystal violet dye [1-4] required an EF up to10^{14} to yield effective cross-sections of 10^{-17} to 10^{-16}, which are comparable to the cross-sections involved in single-molecule fluorescence spectroscopy. These studies employed colloidal Ag as the SERS metal and the largest enhancements were observed with scattering from molecules interacting with individual Ag nanoclusters. The types of nanostructures required to produce such large EFs were modeled in the theoretical work of Xu et al. [3,4]. This work showed that enhancements in excess of 10^3 required the interaction of two nanoparticles in very close proximity or the interpenetration of two nanoparticles to form a nanocluster. Molecules situated in the crevice between two particles or at the crevice of a nanocluster could experience EFs up to 10^{11} due to optical field effects. Assuming a typical intrinsic cross section of 10^{-30} cm^2, the additional factor of 10^3 to produce an EF of 10^{14} was attributed to chemical resonance effects at the excitation wavelength.

These single nanocluster results are very exciting because they demonstrate the potential of SERS as a highly sensitive, chemically specific diagnostic technique. However, the application of SERS as the basis for a highly reliable, highly reproducible detector system cannot rely on the fortuitous location of a highly effective single nanocluster under a microscope objective. Such application requires a deliberately constructed, nanotextured surface that incorporates a very high density of metallic nanostructures that incorporate the proper size, shape, and spacing to produce large EFs so that most of the molecules one wishes to detect will experience high optical fields and scatter with sufficient intensity to be detected.

In view of the goal of incorporating SERS-based detectors directly within the microfluidic channels of microchromatographs, initial work concentrated on technologies that were compatible with direct integration. To achieve this objective, a template was needed to control the size and spacing of Au or Ag deposits within a microchannel. The approach selected was based upon evaporative deposition of Al in the detector regions of the microchannel, partial anodization of the aluminum to form a template, electrodeposition of Au or Ag nanostructures that provide the SERS enhancement, and capping of the detector region with an optically transparent silicon oxynitride process that employs a sacrificial photoresist to form hollow microducts.

The template is formed by the anodization of Al to form a matrix of essentially vertical nanopores extending from the underlying aluminum substrate to the surface [5]. This is shown in the scanning electron micrograph (SEM) in Fig. 1.

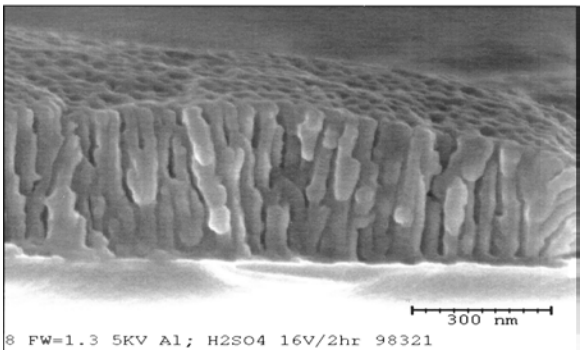

Figure 1. Side-view SEM micrograph of anodized aluminum surface.

A surface view of a typical anodized template is shown in Fig. 2. The spacing and size of the nanopores are fairly regular but not perfectly so. This is less than ideal from the perspective of achieving a uniformly high EF over the laser excitation area.

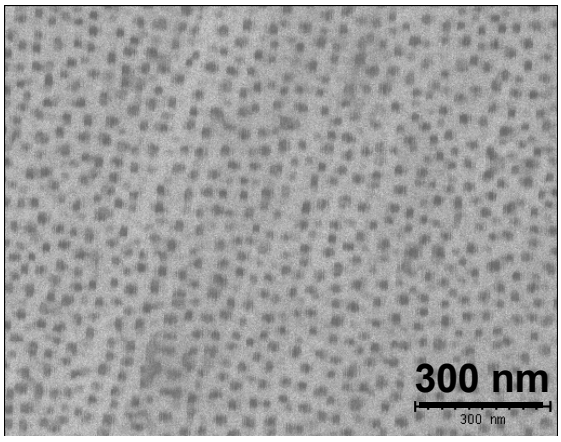

Figure 2. Surface view SEM micrograph of anodized alumina template.

Anodization conditions employing phosphoric acid solutions have been identified that can reproducibly provide 6-9 nm pores spaced 30-40 nm apart, 16-20 nm pores spaced 60-80 nm apart, and 70-90 nm pores spaced 70-90 nm apart. The most desirable range of pore sizes and pore separations would depend on the nanostructure of the Au or Ag electrodeposits that are to be grown out of the pores. Two different anodization textures are shown in Fig. 3, where the second texture is obtained by removing an initial layer of anodic oxide followed by reanodization.

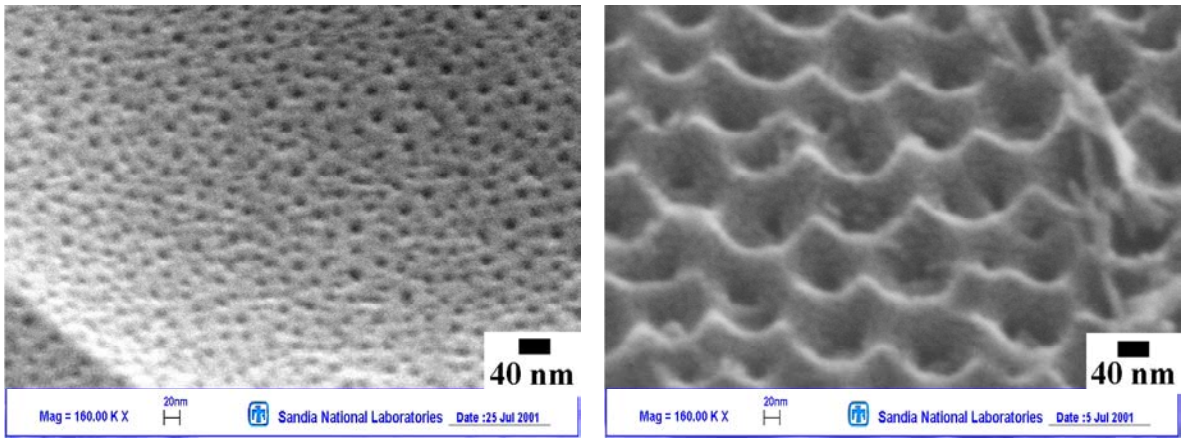

b) a)

Figure 3. Surface view SEM micrographs of anodized aluminum. a) initial texture and b) texture following oxide removal and reanodization.

Au or Ag nanowires can be electrodeposited in the nanopores to provide an array of spheroids that first emerge from the nanopore and then grow laterally across the alumina. Fig. 4 is an SEM of Au nanowires electrodeposited through a polyester ion-track membrane with pore sizes of 100 nm. There are many small wires emerging from the nanopores, but there are also a few structures that are much larger. This phenomenon is characteristic of plating solutions without organic additives called levelers that retard deposition at regions with higher rates to permit the deposition at regions with slower rates to keep pace. Rates within the nanopores, where reactant availability is more limited, are slower than those above the surface. Consequently, those wires that emerged earliest from a pore grew faster than those still in the pores, resulting in micrometer-scale features rather than nanometer-scale ones. As a consequence of preferential growth of the early-emerging wires in plating solutions without levelers, the uniform surface desired for close-proximity crevice formation from adjacent nanowires was not achieved in these growths. Further experimentation with different solution compositions containing organic compounds that serve as levelers may solve this problem and produce a more uniformly nanoscale surface.

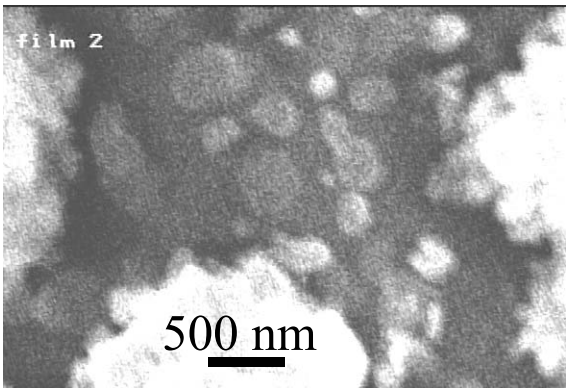

Figure 4. SEM micrograph of Au nanowires emerging from membrane template.

In addition to microchannel-compatible approach described above, some surfaces were examined for SERS efficiency that were not compatible with microchannel requirements but which would be suitable for detectors attached to standard chromatograph. One particularly successful surface was designed to test the effectiveness of close-packed hemispheres that would be expected to provide enhancement factors up to 10^7 according to the Xu model. Figure 5 shows an array of 200 ±10-nm polystyrene beads prior to being coated with 41 nm of Ag to form a SERS surface. While many beads are close or even touching in places, it is clear that the typical spacing between beads is not less than 5 nm, as would be required for the largest enhancements calculated for such structures by Xu et al.

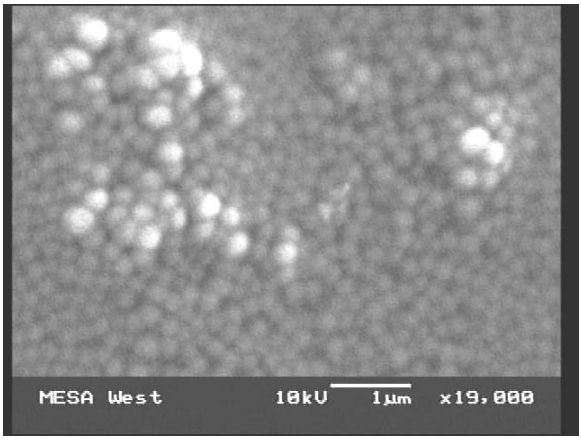

Figure 5. SEM micrograph of polystyrene bead substrate for Ag SERS surface.

Raman spectra were obtained in this study using incident light at 514.4 and 632.8 nm. Laser powers less than 10 mW were coupled into the central fiber of an optical fiber bundle and positioned above the candidate SERS surface at a distance that optimized the pick-up of scattered light by a circular array of fibers surrounding the central fiber. Laser powers were employed for all measurements to reduce possible surface damage due to heating.

Pyridine was employed as the SERS-active compound for testing the surfaces. The chemical bonding of the nitrogen atom in pyridine with metals such as Ag induces a shift in the vibrational frequencies relative to those found in an unbound molecule.

Consequently, an estimate of the effective cross section can be made from the intensity of the shifted peaks assuming a monolayer is bound ($4x10^{14}$ molecules/cm^2).

The elastic Rayleigh scattering of the atomic emission from the laser plasma can be used to quantify the inelastically scattered light. A plasma line at 675 nm (1004cm^{-1}) lies between the two main SERS peaks from the bound pyridine and was used to estimate the scattering efficiency. Using neutral density filters to reduce the intensity of the main laser line sufficiently to permit safe illumination of the CCD detector array, the ratio of intensities of the 675-nm plasma line to the 633-nm laser line was determined to be $2x10^{-10}$. To achieve a Raman scattering intensity from 10^{14} pyridines/cm^2 that is comparable in intensity to the plasma line, a scattering cross-section on the order of 10^{-22} cm^2 is required.

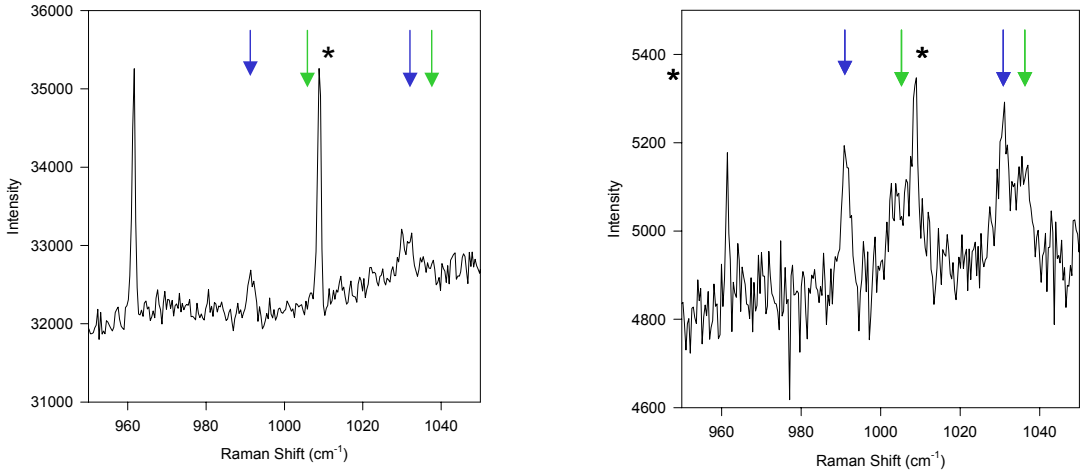

(a) **(b)**

Figure 6. Raman spectra of pyridine in contact with Ag-coated polystyrene beads.

The SERS spectra of pyridine in contact with Ag-coated polystyrene balls is shown in Fig. 6 with the key Raman peaks indicated by arrows and the reference plasma line by the asterisk. The intensity of the elastically scattered plasma line at 1004 cm^{-1} provides a measure of the efficiency of collection of scattered light from the textured surface. Smooth, near-specular surfaces produce the highest intensity Rayleigh lines while highly dendritic surfaces serve essentially as blackbody absorbers that scatter virtually no intensity into the Raman optical system. The difference in intensity of the Rayleigh lines in Figure 6 is related to this phenomenon. The spectrum in Fig. 6(a) corresponds to the surface shown in Fig. 5. It is dominated by the peaks from bulk pyridine at 991 and 1031 cm^{-1} with only a hint of possible surface-bound pyridine at 1001 and 1035 cm^{-1}. The surface that generated the spectrum in Fig. 6(b) consisted of polystyrene balls that had been annealed at 60 °C to induce some plastic flow while retaining a generally nanospherical shape. After annealing, the beads that were formerly not touching should be in contact to produce the narrow crevices that are expected to produce large local field enhancements. The beads were then coated with Ag. This surface produced strong peaks at the frequencies corresponding to surface-bound pyridine. The intensity of these peaks relative to the laser plasma line at 1004 cm^{-1} is

consistent with a cross-section on the order of 10^{-22}. Enhancement of the intensity from free pyridine in close proximity to the surface is also seen. Since pyridine is a relatively weak Raman scatterer ($\sigma_0 \approx 10^{-30}$-$10^{-29}$), this corresponds to an enhancement factor of 10^7 to 10^8. Similar values were predicted by the Xu model for 140-nm spheres separated by 5.5 nm.

The calculations of Xu et al. suggest that the enhancements can be increased even more (to 10^{11}) by further reducing interparticle spacing to 1 nm or by the presence of sharp protrusions. Fabrication efforts to produce such surfaces were ended by termination of funding.

Protein Separation Microchromatography

A novel UV-initiated acrylate-based porous polymer monolith was developed during the first year as a stationary phase for wafer-scale electrochromatography of cationic, anionic, and neutral amino acids and peptides. These monoliths are cast-to-shape, and are tunable for charge and hydrophobicity (Fig. 7.) For separations at low pH, monoliths containing quaternary amine moieties were used to achieve high electroosmotic flow, and for high pH separations monoliths with acidic sulfonic acid groups were employed. Efficient and reproducible separations of amino acids and native peptides were achieved using both negatively and positively charged polymer monoliths in capillaries [6]. Separation efficiencies in the range of 65000-371000 plates/m were obtained. The monoliths were also cast in the microchannels of glass chips and electrochromatographic separation of three bioactive peptides was obtained.

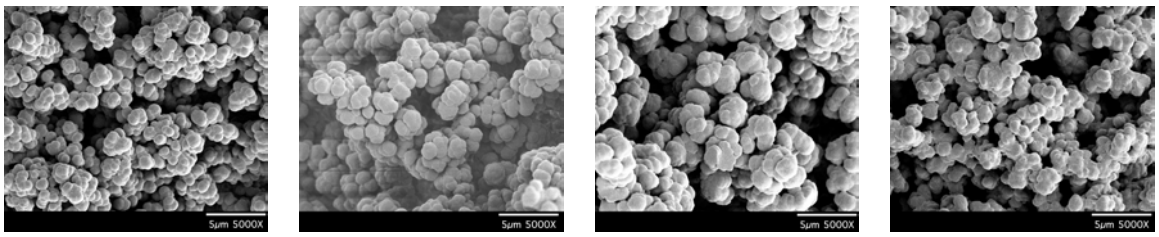

(a) (b) (c) (d)

Figure 7. SEM micrographs of porous polymer monoliths. Methanol-extracted samples of (a) negatively-charged lauryl monolith, (b) positively-charged butyl monolith, (c) positively-charged butyl monolith with double the percentage (1%) of charged monomer, and (d) positively-charged butyl monolith with 1% cellulose.

An important addition to the protein chromatographic system was made during the second year by the creation of acrylate-based porous polymer monoliths that can serve as protein preconcentrators to reduce the optical system sensitivity required to detect and identify a particular protein, such as a bacterial toxin. The protein preconcentrator is based on a polymer that effectively serves as a protein electrokinetic (EK) trap. This polymer, when synthesized in a capillary tube or in a microchannel, selectively traps protein analytes from complex mixtures injected in the polymer by the electroosmotic flow of a suitable solvent. The trapped proteins can subsequently be released from the polymer matrix by the pressure-driven flow of the same buffer. Figures

8(a) and 8(b) show a simple experiment in which α-lactalbumin is trapped electrokinetically and subsequently released under pressure-driven flow.

The protein-trapping polymer is an acrylate-based porous sol-gel that is also a cast-to-shape, photopolymerized monolith. The polymer is synthesized in two separate, orthogonal steps: 1) the polymeric backbone and other permanent structures, as well as the microporous character of the monolith are established and 2) alkoxysilicon moieties are hydrolyzed under mild acidic conditions to generate negatively-charged groups on the surface of the monolith in order to support electroosmotic flow.

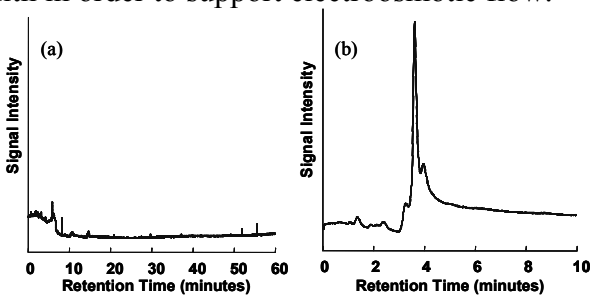

Figure 8. Electrokinetic (EK) trapping (a) and release (b) of α- lactalbumin (0.1 mg/mL)

In addition to trapping proteins, the photopolymerized sol-gel has been shown to serve as an efficient on-line preconcentrator of small molecules. One example is thiourea, a species that is usually unretained in reversed-phase chromatographic analyses. The preconcentration of thiourea was demonstrated by systematically increasing the injection times of a thiourea sample while maintaining a constant applied voltage. Under the proper operating conditions, the total peak area of the thiourea signal increases with increasing injection times. Furthermore, the increase in peak area is a result of an increase in peak height with virtually no change in peak width, consistent with an increasing concentration of the sample plug. This work has generated a patent application entitled Electrokinetic Trapping of Proteins on Cast-to-Shape Media, SD-8363.

The electrokinetic trapping technology has potential applications for the analysis of biotoxins. The use of the monolithic sol-gel in a capillary tube or in a microchip could enable the sampling and preconcentration of trace amounts of bioactive proteins for analysis in portable devices. This type of sol-gel monolith has been previously shown to exhibit reversed-phase behavior in pressure-driven chromatographic analysis. Therefore, its trapping characteristics could be directed towards the isolation of proteins from complex mixtures and a subsequent, *in situ*, pressure-driven chromatographic separation. Another plausible scenario is that in which a protein-trapping element could serve as a reactor, *i.e.*, a region in a capillary tube or in a microchip where proteins could be isolated, chemically modified, released and analyzed in a temporally resolved fashion. In addition to temporal resolution, one could envision a spatial resolution in the analysis of an isolated protein sample *via* a mobile electrokinetic trapping element. This element would serve as a "protein carrier" by transporting previously isolated analytes to remote regions of a microchip, where they can subsequently be released and analyzed. This action could also be carried out in a stepwise fashion, where portions of an isolated protein sample are distributed among different regions of a microchip for simultaneous,

parallel analysis. Finally, by combining the features discussed above in a microchip (electrokinetic trapping, on-line preconcentration, and the possibility of a sol-gel monolith with mobile character) it would be possible to deliver protein analytes to a variety of downstream analytical methods with both spatial and temporal control, as well as control of analyte concentration.

References

1. K. Kneipp, Y. Wang, H. Kneipp, L.T. Perelman, I. Itzkan, R.R. Dasari, and M.S. Feld, Phys. Rev. Lett. **78**, 1667 (1997).
2. K. Kneipp, H. Kneipp, V.B. Kartha, R. Manoharan, G. Deinum, I. Itskan, R.R. Dasari, and M.S. Feld, Phys. Rev. E **57**, 6281 (1998).
3. H. Xu, E.J. Bjerneld, M. Käll, and L. Börjessen, Phys. Rev. Lett. 83, 4357 (1999).
4. H. Xu, J. Aizpurua, M. Käll, and P. Apell, Phys. Rev. E **62**, 4318 (2000).
5. W.G. Yelton, K.B. Pfeifer, and A.W. Staton, J. Electrochem Soc. **149**, H1, (2002).
6. R. Shediac, S.M. Ngola, D.J. Throckmorton, D.S. Anex, T.J. Shepodd, and A.K. Singh, J. Chromatog. A **925**, 251 (2001).

Distribution:

4	MS1425	Carol I. Ashby	1744
3	MS9403	Timothy J. Shepodd	8722
2	MS1425	W. Graham Yelton	1743
2	MS1425	David J. Muron	1744
1	MS0188	LDRD Office	1011
1	MS9018	Central Technical File	8945-1
2	MS0899	Technical Library	9616
1	MS0612	Review & Approval Desk for DOE/OSTI	9612

Journal of The Electrochemical Society, **149** (1) H1-H5 (2002)
0013-4651/2001/149(1)/H1/5/$7.00 © The Electrochemical Society, Inc.

Porous Al_2O_3 Nanogeometry Sensor Films

Growth and Analysis

W. G. Yelton,* K. B. Pfeifer,*,z and A. W. Staton

Sandia National Laboratories, Albuquerque, New Mexico 87185-1425, USA

Material studies of thin films of porous anodized Al_2O_3 have been undertaken to determine their applicability as sensing films for application on surface acoustic wave sensors. We describe the production of these films including their growth parameters and provide an analysis of their crystal morphology. These films were then exposed to various concentrations of analyte and their surface areas determined using Brunauer-Emmett-Teller-type analysis. Finally, the surface area as a function of anodization potential is provided for the films.
 [DOI: 10.1149/1.1421608]

Manuscript submitted April 16, 2001; revised manuscript received September 6, 2001. Available electronically November 27, 2001.

Recent efforts have focused on the chemical and physical diversity of interface materials for surface acoustic wave (SAW) technology.[1] These materials provide SAW sensors with their analyte selectivity. Issues of wide dynamic range and high sensitivity must also be addressed for sensor arrays to compete in applications requiring low detection limits such as the development of sensor systems useful in the detection of chemical plumes for security applications. Each chemical sensor consists of interdigital transducers patterned on the surface of an ST-cut quartz substrate with a thin-film coating placed in the SAW propagation path to perturb the acoustic wave velocity during analyte sorption. Since no single coating provides absolute analyte specificity, an array of sensors provides a high degree of discrimination ability. By providing a diverse set of material coatings, the sensor array offers a degree of chemical sensitivity and selectivity. Because SAW devices respond in proportion to change in mass per nominal unit area of the device surface, sensitivity is enhanced by surface modification with high area, thin-film coating materials to allow a greater mass of analyte adsorption at a given ambient concentration. A number of anodization studies in the literature have dealt primarily with bulk materials and their resultant properties, which are significantly different from evaporative deposited thin-film systems.[2,3] Other studies have dealt with the growth of porous alumina films formed on foil templates.[4] This study deals with porous films grown *in situ* on a sensor substrate where the pore morphology and pore size is controlled by the substrate temperature and the anodization conditions.

Material studies of thin (<1 μm), high surface area, metal/oxide films developed to improve SAW sensitivity, reveal common factors that, in fact, diminish sensor sensitivity. These factors include nonuniformity in the density of the material, the rigidity of the microstructure, and nonuniformity in the thickness of the coating. For example, films developed from high density materials such as Pt, Pd, or Au, have yielded higher dendritic nanogeometries but suffer greater insertion losses for a given thickness. In contrast, because of its low density, microstructure rigidity, ordered porosity, and controllable pore volume, anodized aluminum (Al_2O_3) formed from evaporated deposition of metallic Al suggests promising films for enhanced sensor sensitivity. In the context of this paper, anodized aluminum and alumina refer to two different coatings. Anodized aluminum is a coating where only part of the evaporated aluminum has been converted to alumina. Under this oxidized layer remains metallic aluminum. For alumina, on the other hand, the evaporative aluminum film has been completely converted to an oxide, no additional aluminum is available for anodizing.

* Electrochemical Society Active Member.
z E-mail: kbpfeif@sandia.gov

Experimental

Growth and deposition.—During physical evaporative depositions, the dominant influence on the final microstructure of an Al_2O_3 coating is strongly linked to the surface mobility of the adatoms, which is affected by the substrate temperature and deposition rate. The microstructure of evaporative films can be viewed in terms of the Movchan-Demchishin model also known as the zone structure model (ZSM).[5] In this model, coatings are deposited under three distinct conditions or ''zones.'' At a constant evaporation rate, the material morphology in each zone can be manipulated by the temperature of the substrate (T_s) onto which the Al is deposited. Zones are classified as zone I ($T_s < 0.3T_m$), zone II ($0.3T_m < T_s < 0.45T_m$), and zone III ($T_s > 0.45T_m$) where T_m refers to the melting point of bulk Al.

In zone I, film growth is more agglomerated with ''islands'' of crystalline structures separated by small columnar voids. Because of low thermal energy, due in part to the relatively low substrate temperature as compared to the melting point of the material, the surface mobility of adatoms is limited. The image in Fig. 1 is a cross-sectional view of an agglomerated structure of alumina formed by the anodizing process of evaporated aluminum on a quartz substrate deposited under zone I conditions. After sulfuric acid (0.5 M) anodization under fixed (16 V) anodic potential, the crystal morphology of the Al_2O_3 in Fig. 1 is characterized by disordered alumina microstructures with low effective surface areas. From tunneling electron microscopy (TEM) analysis, these agglomerated oxides reveal tortuous pore openings with diameters on the same order as films developed under zone II conditions, but with limited pore length and corresponding limited pore volume. These features are not visible with high resolution scanning electron microscopy (SEM) examination.

Anodization.—Figure 2 is the cross section of an alumina film formed by the anodizing process of evaporated aluminum grown under zone II conditions. The initial film was vapor deposited under the same conditions as the film in Fig. 1, except that the substrate temperature was held at $0.4\ T_m$. Under zone II conditions, film growth occurs with greater adatom mobility, and favors columnar grain structures with dense intercrystalline boundaries that extend through the coating thickness. The anodization conditions were identical for both films and consist of mounting an Al coated SAW device to a rigid Teflon fixture that was centered in a 250 mL beaker 1 cm from a Pt counter electrode. Electrical contact to the Al film was made through a 1 mm Ti wire mounted on the Teflon fixture. DC resistance was observed at the Ti wire tip (opposite the Ti/Al contact) and a point on the Al surface. If the resistance was 3 Ω/cm^2 or higher, the contact points were filed and cleaned and then the resistance was rechecked.

Prior to entering the solution, power was activated to the electrochemical cell. Before and during the anodizing process, N_2 gas was bubbled through the anodizing solution in front of the SAW

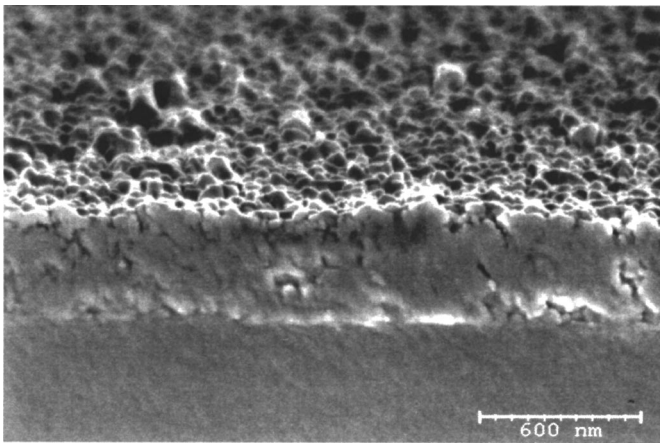

Figure 1. SEM cross section of an alumina film formed by anodizing (16 V applied) evaporated aluminum that was thermally evaporated on quartz at low temperature of 53°C substrate temperature (0.08 T_m). Because of low adatom mobility, the microstructure of the deposit is more agglomerated with voids.

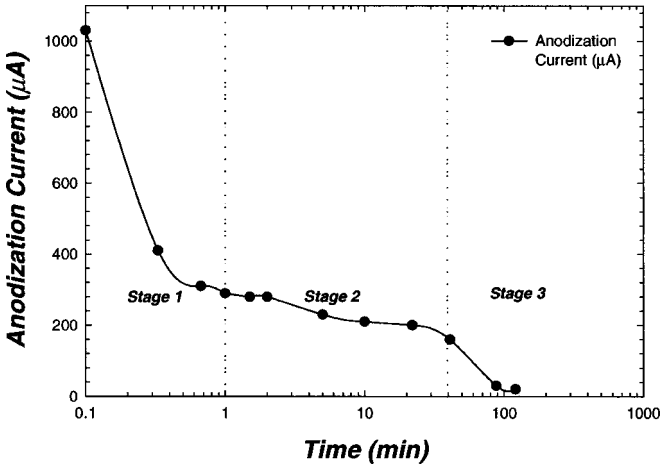

Figure 3. The current decay of 500 nm aluminum evaporated film during constant potential anodization. Solid line is a spline fit of the data as guide to the eye. Note that the current asymptotically approaches a constant value at the end of the stage 3 growth.

device. The N_2 helped to agitate the solution, and for small surface areas, was sufficient for maintaining the temperature of the cell. The samples in Fig. 1 and 2 were anodized at a constant potential of 16 V. For all samples anodized at potentials from 2-25 V, we used 0.5 M H_2SO_4 as the electrolyte. Samples used for the adsorption study were prepared under zone II conditions and anodized for 40 min. These 500 nm films were completely converted to alumina. At these exposures, the finished film thickness ranged from 550-620 nm depending on the driving potential, with higher potentials yielding thicker films and larger pore diameters. Films anodized much longer (stage III) were thinner than the initial 500 nm seed layer with larger pore diameters for a given fixed potential, as compared to alumina films formed under identical conditions but for shorter anodizing times.

Figure 2 reveals straight ordered columns extending from the surface to the substrate. This scanning electron micrograph (SEM) is viewed using a 300 nm scale to clearly reveal the ordered columnar structure in contrast to Fig. 1, which is viewed from a slightly macroview (600 nm scale) to reveal the disorder surface as well as the cross-sectional structure.

The graph in Fig. 3 reflects the current decay over time as an aluminum film, formed under zone II evaporation, is anodized under constant potential. As the aluminum oxide forms, the surface resistance of the film increases dramatically. The solid line in Fig. 3 is a guide for the eye. The film undergoes three stages of change under potentiostatic mode. During the first (growth) stage (the first 60 s in this example), the current drops at a rapid rate, indicating that the nucleation of oxides and crystal structure ordering of the Al_2O_3 is occurring. During the second stage (see Fig. 4), SEM micrographs at 1, 3.5, and 10 min reveal the formation of the oxide with increasing depths as a function of time. From zone II deposition, the unanodized aluminum film evaporated on quartz appears quite rough with a number of large voids. After 60 s of anodization with an applied potential of 10 V, a uniform oxide of 100-150 nm consumes and covers the surface. At 3.5 min, more that 25% of the aluminum is consumed. When 10 min have passed, most of the available aluminum is gone.

As anodization time increases, the thickness of the oxide film grows, consuming and converting the aluminum underlying to an oxide. During stage II (see Fig. 3), the current is fairly stable and the general morphology of the crystal structure in now ordered and the remaining aluminum is converted to oxides by the slow diffusion of oxygen through the thicker oxide film above. During this second stage, the porous film reaches its highest level of impedance for a given overall thickness.

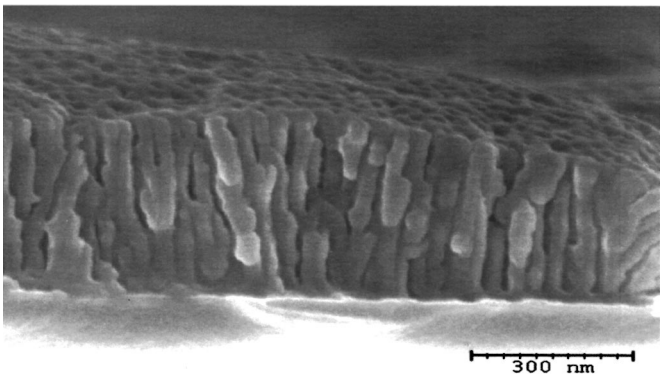

Figure 2. Fractured SEM cross section of an alumina film formed by anodizing (16 V applied) evaporated aluminum. The aluminum was thermally evaporated on quartz at 250°C substrate temperature (0.4 T_m). Due to increased adatom mobility, the microstructure of the deposit is more columnar with distinct intercrystalline boundaries.

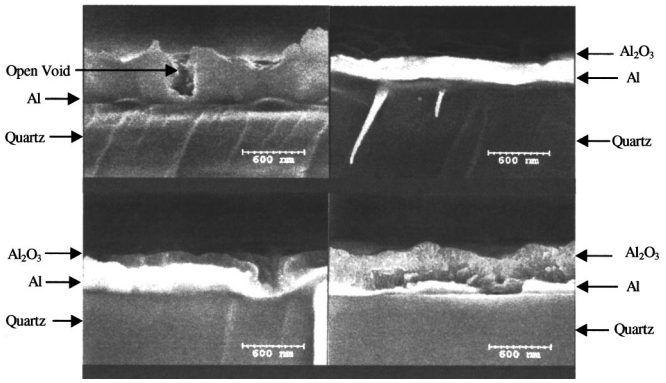

Figure 4. SEM cross sections of films that have been anodized for various times. The four images are viewed from samples that were fractured to reveal cross sections of aluminum oxide, aluminum, and the quartz substrate. The unanodized film is in the upper left-hand corner and proceeding clockwise the photographs are 1, 10, and 3.5 min. All films were deposited under zone II conditions and were anodized at a 10 V potential.

Table I. Table of pore diameter compared to applied potential and anodization time. Data was obtained from SEM micrographs that were near the resolution limit for the smaller pores. However, the general trend toward larger pores with larger applied potential is illustrated.

Applied potential (V)	Time (min)	Pore diameter (nm)
3	125	12 ± 2
10	1	7 ± 2
10	60	10 ± 2
10	200	17 ± 3
12	120	20 ± 5
16	120	30 ± 10

For a film of 500 nm thickness, when anodized at a potential of 10 V, the evaporated bulk aluminum was completely consumed after approximately 40 min corresponding to the observed drop in current illustrated in Fig. 3. During stage III (see Fig. 3), the elemental aluminum has been consumed and converted to oxides. SEM micrographs at 60 and 105 min (not shown) reveal discreet columnar ordering of the oxide down to the supporting quartz substrate.

Table I is a summary of the pore size data obtained from the experiment compared to the applied potential and anodization time. This data was obtained by measuring the pore sizes from SEM photos of the anodized films. Each measurement was obtained by making six to seven measurements from a level section of the coating while avoiding the grain boundaries. An attempt was made to pick points in clusters that represented the bulk surface finish. Since each surface has mountain and valley-like features, the measurements were made on flat mountain-like mesas. At these points, the low voltage (<10 V) formed oxides had similar pore sizes and very little variance. The limited variance in pore size measurements is the result of the SEM resolution. However, at larger voltages, larger pores were very clear and easily measurable. Table I illustrates the trend for larger pore size resulting from higher applied anodization potentials.

Figure 5 illustrates the surface of four aluminum films. The unanodized film, scaled at 600 nm, reveals large grain structures with two voids centered among the cluster of grain structures. Viewed at 200 nm, the surface is covered with pores within 60 s of the beginning of the anodization process. From the plane view after 60 min, the pores

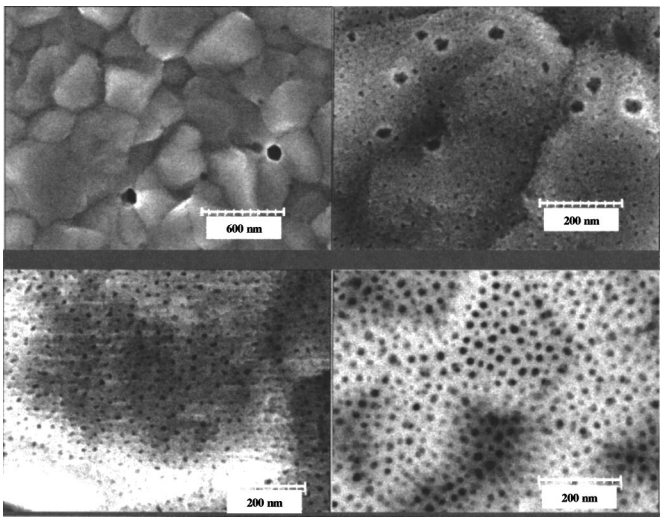

Figure 5. SEM photograph of Al_2O_3 surface as a function of anodization potential. Clockwise from the upper left-hand corner the films are unanodized, anodized for 1 min at 10 V, anodized for 200 min at 10 V, and anodized for 60 min at 10 V. These photos illustrate that after 60 min of anodization, the films are etched by the process and begin to open the pores.

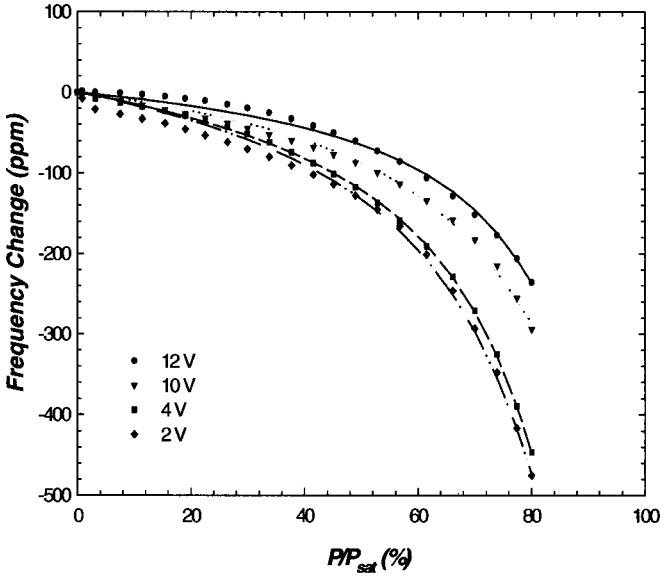

Figure 6. Plot of frequency change *vs*. concentration (P/P_{sat}) for EtOH on SAW devices with Al_2O_3 films produced by the described process. Each curve represents a different anodization voltage and the lines are modified BET fits to the data.

are uniformly spaced with uniform pore openings (*ca*. 10 nm). At 105 min (not shown), the pores remain fairly uniformly spaced but the pore openings at the surface begin to show signs of widening. From a cross-sectional view of this film, the columnar structures are showing signs of separation at the surface. In this final stage of the process, the current in Fig. 3 drops off at an accelerated rate. During this stage, the film is no longer highly conductive as when there was a source of electroactive aluminum available, and the acid electrolyte surrounding the film in the anodizing solution now acts as an etchant. As the film is continuously exposed to the acid electrolyte, the pores are widened and the film becomes thinner. Even though the supporting electrolyte is able to maintain a small flow of current between electrodes, the current is converging asymptotically to a constant value. In Fig. 5, the SEM micrograph of a film processed at 200 min reveals wider pore openings (*ca*. 20 nm), and a breakdown in structure uniformity, along with a thinner overall film thickness.

Analysis

A series of metallic Al films were vapor deposited (500 nm) on SAW devices and anodized at various applied potentials (2-12 V) for 40 to 60 min. The pore diameters measured from SEM micrographs for samples prepared at 2 V are *ca*. 7 nm, and for samples anodized at 12 V are *ca*. 20 nm. A fractured cross section of a film is shown in Fig. 4.

The functionality of these films as sensors was tested. Each SAW device was used as the feedback element of an oscillator circuit operating at approximately 97 MHz. The frequency outputs from the oscillators were then measured using a frequency counter. Figure 6 is the frequency shift of four SAW devices during the adsorption of ethanol at increasing normalized vapor pressures. Insertion losses for these coated devices were less than 1 dB greater than for a bare device, but film sensitivity increases were of an order of magnitude over a bare device. A decrease in pore size yielded an increase in sensitivity.

The modified adsorption model of Brunauer, Emmett, and Teller (BET)[6,7] has been applied to the problem of measurement of heat of adsorption and surface area for the sensitive films of Al_2O_3 created using processes described above. The films were formed on ST-cut quartz[a] SAW devices and the adsorption of ethanol (EtOH) was

[a] ST-cut quartz is a singly rotated cut having Euler angles $\lambda = 0°$, $\theta = 90°$, and $\mu = 132.75°$.

measured. The adsorption isotherms were then fit using the Marquardt-Levenberg algorithm to extract the values of the heat of adsorption of the first monolayer onto the surface and the limiting number of surface layers adsorbed.[8] This information was then compared to published values for the heat of adsorption and the surface areas of the films was estimated and compared to the preparation conditions.

The BET adsorption model is a widely accepted technique for experimentally determining the surface area and heat of adsorption of the first monolayer of adsorbate onto a surface.[7] BET measurements are routinely made with N_2 as the adsorbate on a surface cooled to 77 K and are used to study the properties of materials ranging from soils to sol-gels.[9-11] N_2 is the adsorbate of choice due to its well known adsorption cross section (16.2 $Å^2$); however, typical instrumentation designed to make BET measurements is limited to bulk materials and does not allow for measurements of thin-film adsorption. The adsorption characteristics of a bulk material may or may not be representative of the adsorption characteristics of thin films made from that material. Previously, SAW technology has been used to make BET measurements of thin silicate-based sol-gel films by adsorbing N_2 in a He matrix onto a test film cooled to 77 K that was deposited on a SAW device.[12] We have used this technique at room temperature to measure the heat of adsorption and surface area of the Al_2O_3 films described in this paper.

The surface acoustic wave sensor system used to make the measurements was similar to the system reported previously.[13] The system used six SAW devices, each with a different film; all were exposed to the same atmosphere of interest at the same time. Each SAW device was used as the feedback element of an oscillator circuit operating at approximately 97 MHz. The frequency outputs from the oscillators were then measured to 1 Hz resolution using a frequency counter (HP5385A). All SAW devices were mounted in a single brass test fixture whose temperature was actively controlled using a liquid flow from a temperature controlled bath (Haake model K). The brass fixture was designed to provide excellent radio frequency (rf) shielding for the test SAW devices and to provide sufficient thermal mass to moderate the frequency changes due to environmental temperature fluctuations.

The SAW device-based oscillators respond to the adsorption of a chemical species by changes in the wave propagation velocity of the film and this is observed as a change in the frequency of the oscillator. The mechanical influences that effect the frequency of a SAW sensor in an oscillating loop can be written as[14]

$$\frac{\Delta\nu}{\nu_0} = -k_m \frac{\Delta\rho}{\rho_0} + k_s \frac{\Delta S}{S_0} + k_\sigma \frac{\Delta\sigma_q}{\sigma_{q0}} + k_\gamma \frac{\Delta\gamma}{\gamma_0} - k_T \frac{\Delta T}{T_0} \quad [1]$$

where ν is the frequency of oscillation, ρ is the surface mass density of material on the surface of the SAW device, S is the modulus of elasticity of the ST-cut quartz, σ is the conductivity of the film, γ is the stress parameter in the sensing film, and T is the temperature of the SAW surface. The values of k are constants for each parameter of the equation, and the subscript 0 refers to the initial conditions of the unloaded sensor. For our films constructed from Al_2O_3 in a temperature controlled environment, the change in all terms except the surface mass density is approximately zero. Therefore, to first order, the wave velocity is reduced as material is adsorbed onto the surface of the device; the frequency change can be written as a function of surface mass change according to the following relationship[12]

$$\Delta\nu = -\eta_m \nu_0^2 \Delta\rho \quad [2]$$

where $\Delta\rho$ is the change in surface mass density due to the adsorption of the adsorbate onto the film, $\Delta\nu$ is the change in frequency due to the adsorbate, η_m is the mass sensitivity factor (1.3×10^{-6} cm^2/g) of the ST-cut quartz substrate,[15] and ν_0 is the baseline frequency of the SAW oscillator (~97 MHz).

Various concentrations of EtOH in N_2 were passed over the sensors and the frequencies were measured at a single temperature (20°C). These isothermal data are illustrated in Fig. 6 as a plot showing the change in the frequency between the initial frequency and the current frequency at a given concentration. The concentration is represented as the ratio between the partial pressure of the alcohol and that alcohol's saturation vapor pressure at the test temperature (20°C). The data points on the plot are the measured data and the solid line is a fit of the data to the modified BET experimental isotherm model. The modified BET model of chemical adsorption postulates that there are two heats of adsorption of the adsorbate onto the film: the larger heat of adsorption is that of the first monolayer binding to the film surface and the smaller heat of adsorption is that of the adsorbate binding to itself (*i.e.*, the heat of vaporization of the adsorbate). The modification of the BET from its initial form is the addition of the parameter n, which is the limiting number of monolayers that will adsorb onto the surface. The pore size or other physical limitations usually determine this limit. The standard BET model is limited in applicability to a concentration range of 0-30% P/P_{sat} where P is the partial pressure of the absorbate and P_{sat} is the saturation vapor pressure of the absorbate; however, the modified form has been shown to have a much greater range of applicability.[8]

It is apparent from Eq. 2 that the change in the number of molecules (ΔN) binding to a surface is proportional to the change in frequency of the SAW oscillator. Therefore, we may write the modified BET equation in terms of frequency changes rather than changes in the number of molecules as is commonly seen

$$\frac{\Delta\nu}{\Delta\nu_m} = \frac{\Delta N}{\Delta N_m} = \frac{c\xi}{(1-\xi)} \frac{1 - (n+1)\xi^n + n\xi^{n+1}}{1 + (c-1)\xi - c\xi^{n+1}} \quad [3]$$

where ξ is the ratio between the partial pressure of the adsorbate and its saturation vapor pressure (P/P_{sat}); $\Delta\nu$ is the frequency change due to the adsorbate at the current partial pressure; $\Delta\nu_m$ is the frequency change due to one monolayer coverage on the surface; c is a constant that depends on the difference in the heat of adsorption between the adsorbate and the surface (Q_1), the heat of vaporization of the adsorbate (Q_ν), the temperature of the surface (T), and the universal gas constant (R)

$$c = e^{(Q_1 - Q_\nu)/RT} \quad [4]$$

The data were fit to Eq. 3 using a nonlinear Marquardt-Levenberg regression algorithm with three adjustable parameters: the monolayer coverage frequency change ($\Delta\nu_m$), the heat of adsorption constant (c), and the limiting number of monolayers adsorbed (n). The heat of adsorption of the first monolayer of EtOH onto Al_2O_3 was estimated from Eq. 4 to be 9.78 kcal/mol (the heat of vaporization for EtOH is approximately 9.67 kcal/mol[16]). The value for the heat of adsorption of EtOH compares favorably to the values found in the literature of 10.1 kcal/mol.[17]

From the single monolayer frequency change ($\Delta\nu_m$), it is possible to estimate the surface area of the film given convenient assumptions. We assume that EtOH is a spherical molecule with a standard area (A_{EtOH}) of 32.5 $Å^2$. This value was found by using the van der Waals constant for the volume occupied by 1 L of molecules and calculating the area. A similar calculation was performed on H_2O as a check of the validity of the method and the area was found to be consistent with the literature value for the standard area of H_2O. The area of the film can then be calculated from the following formula

$$A_{film} = \frac{-\Delta\nu_m A_\nu}{\nu_0^2 \eta (MW_{EtOH})} A_{EtOH} \quad [5]$$

where A_ν is Avogadro's number and MW_{EtOH} is the molecular weight of ethanol (46 g/mol).

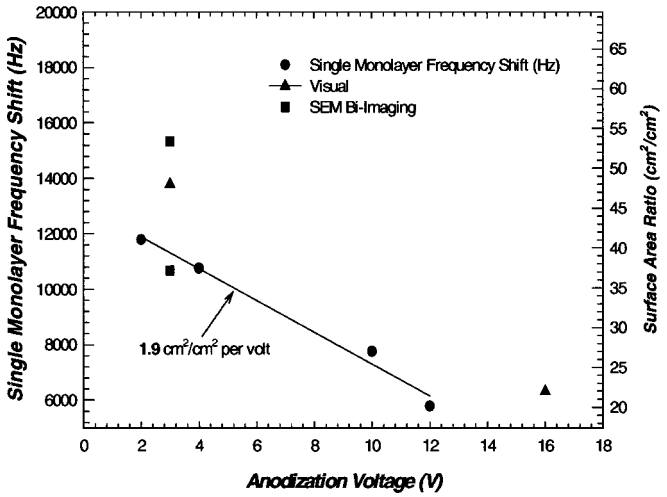

Figure 7. Plot of single layer frequency shift as a function of anodization voltage. The right-hand axis is scaled to provide the ratio of film surface area as a function of anodization voltage. (●) Indicates the SAW data. (■) Are data obtained from SEM bi-imaging measurements of similarly grown films. (▲) Are measurements made by visually examining SEM photographs of the films and calculating the surface area from the pore density, pore diameter, and known film thickness.

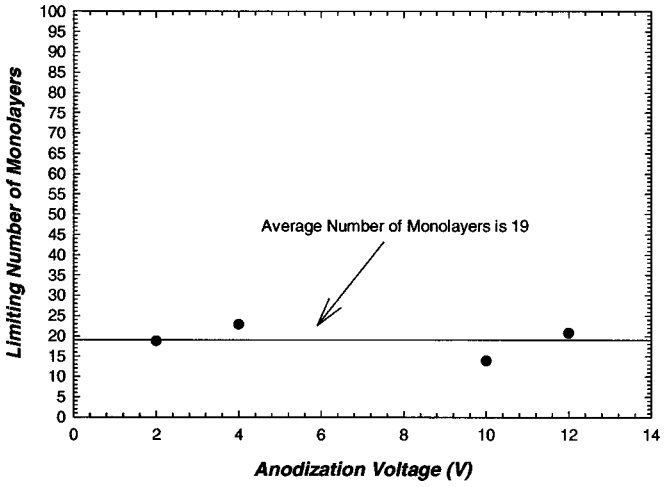

Figure 8. Plot of average number of monolayers that form on the surface of the films as determined from a fit of the data to the BET model. While the average value ($n = 19$) is inconsistent with the number that is calculated to fit in a pore (assuming a diam of 0.6 nm) as found from the spherical model, the results found for the surface area are calculated from the single monolayer response and are therefore, consistent.

We have plotted the single monolayer frequency change as a function of anodization potential in Fig. 7. From these data, we can estimate the change in surface area as a function of anodization voltage. In addition, we have estimated that the film formed at 2 V anodization potential has a surface area of about 40 (cm^2/cm^2) and the surface area decreases at a rate of 1.9 (cm^2/cm^2) for each 1 V increase in potential. The nomenclature A (cm^2/cm^2) implies that for every 1 cm^2 of planar coverage, the film has A cm^2 of actual surface area. The surface areas of several similar films were measured using other techniques, including SEM bi-imaging and manually computing the surface area by measuring the pore diameter from an SEM image and assuming a cylindrical pore of known depth. Both of these techniques compare favorably with the BET technique as is clear from Fig. 7.

The parameter n has an average value of 19 layers for all of the films tested (Fig. 8). Our SEM measurements of pore size indicate that the pores of the samples tested are between 7 nm and 20 nm in diam for films in the 2 and 12 V range; the diameter of the spherical EtOH model is on the order of 0.64 nm. Thus, 19 monolayers of rigid spherical molecules will not fit in the pores. Thus, we might conclude that the packing density of the molecules is higher when packed into the pores increasing the average number of monolayers on the surface. However, the value of n is not critical to the calculation of the surface area since surface area is derived from the single monolayer coverage value. Thus, the surface area value reported is unaffected by this inconsistency in the modeled results.

Conclusion

Thus, we have illustrated the utility of a surface acoustic wave analysis of the surface area of thin films formed by anodizing metallic Al films that were deposited under greater surface mobility (zone II conditions). We have calculated the surface area and found that for every 1 V decrease in anodization potential the surface area of the film increased by 1.9 (cm^2/cm^2) over the range tested. This rate will not continue at either the lower or upper limits of potential; however, over this somewhat limited range of applicability the film grower can engineer the surface area to controllable values.

The general conclusion from this study suggests that complete film anodization under a low potentiostatic mode is reached near the end of the second stage. Continued exposure of the film in the acid electrolyte during the third stage only deteriorates the columnar morphology. In addition, we have measured the surface area of the films by measuring the adsorption isotherms of the films and extracting the surface area and heat of adsorption using the modified BET model of adsorption. The results indicate that the heat of adsorption of the first monolayer is 9.78 kcal/mol and the surface areas decrease over the values of potential tested at a rate of -1.9 (cm^2/cm^2)/V. This allows the film surface area to be engineered to a precise surface area as desired. These types of studies will allow further development of chemically sensitive films for application in detection, quantification, and speciation of unknown chemical plumes found in the environment.

Acknowledgment

Sandia is a multiprogram laboratory operated by Sandia Corporation, a Lockheed Martin Company, for the United States Department of Energy under contract DE-AC04-94AL85000.

Sandia National Laboratories assisted in meeting the publication costs of this article.

References

1. A. J. Ricco, G. C. Osbourn, and R. M. Crooks, *Acc. Chem. Res.*, **31**, (1998).
2. H. Asoh, K. Nishio, M. Nakao, T. Tamamura, and H. Masuda, *J. Electrochem. Soc.*, **148**, B152 (2001).
3. J. P. O'Sullivan and G. C. Wood, *Proc. R. Soc. London*, **317**, (1970).
4. C. Miller and M. Majda, *J. Electroanal. Chem.*, **207**, 49 (1986).
5. B. A. Movchan and A. V. Demchishin, *Phys. Met. Metallogr.*, **28**, 83 (1969).
6. S. Brunauer, P. H. Emmett, and E. Teller, *J. Am. Chem. Soc.*, **60**, 309 (1938).
7. A. W. Adamson, *Physical Chemistry of Surfaces*, p. 538, John Wiley & Sons, New York (1982).
8. K. B. Pfeifer, *Langmuir*, **11**, 4793 (1995).
9. C. T. Chiou, *Environ. Sci. Technol.*, **24**, 1164 (1990).
10. W. Wagner, R. S. Averback, H. Hahn, W. Petry, and A. Wiedenmann, *J. Mater. Res.*, **6**, 2193 (1991).
11. R. Tsunoda, *J. Colloid Interface Sci.*, **130**, 1,60 (1989).
12. A. J. Ricco, G. C. Frye, and S. J. Martin, *Langmuir*, **5**, 273 (1989).
13. R. W. Cernosek, W. G. Yelton, C. W. Colbum, L. F. Anderson, A. W. Staton, G. C. Osbourn, J. W. Bartholomew, R. F. Martinez, A. J. Ricco, and R. M. Crooks, in *Chemical Microsensors and Applications* II, SPIE, Vol. 3857, p. 147 (1999).
14. S. L. Hietala, Ph.D. Dissertation, University of New Mexico (1997).
15. D. S. Ballantine, R. M. White, S. J. Martin, A. J. Ricco, E. T. Zellers, G. C. Frye, and H. Wohltjen, *Acoustic Wave Sensors: Theory, Design, and Physico-Chemical Applications*, p. 74, Academic Press, San Diego, CA (1996).
16. *Handbook of Chemistry and Physics*, 44th ed., p. 2412, CRC Press, Boca Raton, FL (1962).
17. P. F. Rossi and P. Rossi, *Adsorption Sci. Technol.* **13**, 215 (1996).

ELSEVIER

Journal of Chromatography A, 925 (2001) 251–263

JOURNAL OF CHROMATOGRAPHY A

www.elsevier.com/locate/chroma

Reversed-phase electrochromatography of amino acids and peptides using porous polymer monoliths

Renée Shediac, Sarah M. Ngola[1], Daniel J. Throckmorton, Deon S. Anex[2], Timothy J. Shepodd, Anup K. Singh*

Chemical & Radiation Detection Laboratories, Sandia National Laboratories, Livermore, CA 94551-0969, USA

Received 20 March 2001; received in revised form 29 May 2001; accepted 6 June 2001

Abstract

Efficient and rapid separation of minute levels of amino acids and bioactive peptides is of significant importance in the emerging field of proteomics as well as in the clinical and pharmaceutical arena. We have developed novel UV-initiated acrylate-based porous polymer monoliths as stationary phases for capillary- and chip-electrochromatography of cationic, anionic, and neutral amino acids and peptides, followed by absorbance or laser-induced fluorescence detection. The rigid monoliths are cast-to-shape and are tunable for charge and hydrophobicity. For separations at low pH, monoliths containing quaternary amine moieties were used to achieve high electroosmotic flow, and for high pH separations monoliths with acidic sulfonic acid groups were employed. Efficient and reproducible separations of phenylthiohydantoin-labeled amino acids, native peptides, and amino acids and peptides labeled with naphthalene-2,3-dicarboxaldehyde (NDA) were achieved using both negatively- and positively-charged polymer monoliths in capillaries. Separation efficiencies in the range of 65 000–371 000 plates/m were obtained with capillary electrochromatography. Buffer composition and the degree of column hydrophobicity were studied systematically to optimize separations. The monoliths were also cast in the microchannels of glass chips and electrochromatographic separation followed by laser-induced fluorescence detection of three NDA-labeled bioactive peptides was obtained.

Keywords: Electrochromatography; Monolithic columns; Stationary phases, electrochromatography; Derivatization, electrochromatography; Chip technology; Amino acids; Peptides

1. Introduction

Achieving high-resolution separations of amino acids and peptides has important implications for amino acid analysis, peptide sequencing, protein structure determination, and the rapidly emerging field of proteomics. High-performance liquid chromatography (HPLC) has been the method of choice for separation of biological molecules [1,2] but recently significant progress has been made towards employing capillary electrochromatography (CEC) for separation of proteins [3–7], peptides [3,5,8,9], and amino acids [10–13]. Electrochromatography, a powerful technique that combines the strengths of

*Corresponding author. Mailstop 9951, Sandia National Laboratories, Livermore, CA 94551-0969, USA. Tel.: +1-925-294-1260; fax: +1-925-294-3020.

E-mail address: aksingh@sandia.gov (A.K. Singh).

[1]Present address: LumiCyte, Fremont, CA 94538-6532, USA.

[2]Present address: Eksigent Technologies, Livermore, CA 94550, USA.

0021-9673/01/$ – see front matter
PII: S0021-9673(01)01036-6

capillary zone electrophoresis (CZE) and liquid chromatography, is especially attractive for development of portable analysis systems as it is readily amenable to miniaturization. Traditionally, CEC has been performed using fused-silica capillaries packed with spherical silica particles. There are a number of drawbacks associated with packed capillaries, such as the time and effort required for packing, the necessity for frits, and the potential leakage of particles. Packing of channels in a chip is considerably more tedious and requires microfabrication of geometrical features to serve as frits. In contrast, in situ casting of polymer monoliths in capillaries and microchannels reproducibly affords relatively uniform packed beds, therefore eliminating the difficulties associated with packing silica beads and the need for retaining frits. The availability of a wide range of monomers enables critical stationary phase properties such as charge and hydrophobicity to be easily tuned to meet the specific demands of separating many types of analytes. In situ polymerization can be thermal- or photo-initiated but the latter has been reported to produce columns with higher separation efficiencies and is also more suitable for casting patterned monoliths in microfabricated channels [8]. In the last few years, owing to their unique properties, porous polymer monoliths have been utilized as stationary phases for CEC, pioneered by Hjertén and coworkers [4,14], and later modified by several groups including Fréchet and coworkers [15–20], Novotny [21], and Horváth and coworkers [7,22,23]. Acrylate-based polymer monoliths developed in our laboratory [24] require a very short (5–20 min) cure time under UV irradiation and support sufficient EOF as cast (no pressure flushing is necessary), making them especially suitable for chip-based application. These materials have reproducibly demonstrated high efficiencies (>150 000 plates/m) for CEC separation of neutral aromatic compounds but their applicability as separation media for charged analytes has not been investigated in detail.

To date, CEC has been predominantly applied to separation of neutral molecules where electrophoretic mobility is not a factor. In CEC of charged molecules, the separation mechanism couples two simultaneous phenomena — the electrophoretic migration of analytes, and the differential partitioning of analytes in stationary and mobile phases. Since biological molecules such as peptides and proteins have multiple ionizable groups that are charged and exhibit varying degrees of polarity, CEC is a potentially powerful tool for their biochemical analysis. In this work, we report the separation of neutral, cationic, and anionic amino acids and peptides by CEC using acrylate-based UV-initiated hydrophobic porous polymers as monolithic stationary phases. Depending on the pH of the mobile phase and the nature of the analytes, either cationic or anionic groups were incorporated into the monoliths for generation of EOF. Selectivity was easily tuned by manipulating the degree of polymer hydrophobicity. Chip electrochromatography using in situ cast polymer monoliths was employed to separate three fluorescently-labeled bioactive peptides, demonstrating the applicability of these materials as separation media in microfluidic devices.

2. Experimental

2.1. Apparatus

Polymerization was performed in a Spectrolinker XL-1500 UV crosslinker (Westbury, NY, USA) operated at 365 nm, according to a procedure described elsewhere [24]. CEC, capillary electrophoresis (CE), and chip electrochromatography experiments were performed using a Bertan 30 kV current-limited, adjustable d.c. power supply (Hicksville, NY, USA). UV absorbance was monitored using a Linear 200 detector (San Jose, CA, USA) set at 214 nm. Laser-induced fluorescence (LIF) detection was performed using a 413 nm krypton ion laser (Coherent, Santa Clara, CA, USA). A chip station was built in the laboratory, and both capillary and chip systems were enclosed in a Plexiglas box fitted with an interlock system to avoid electrical shock. The laser was focused onto the detection window of the capillary or the microchip and fluorescence was collected perpendicular to the incident beam by using a high numerical aperture microscope objective (Nikon) having 40× magnification, an NA of 0.85, and a 0.37 mm working distance. The background fluorescence and the scattered light were minimized by using a long-pass filter

and a variable slit. The fluorescence was collected by a photomultiplier tube (PMT; Hamamatsu, Japan) and the signal was amplified with a lock-in amplifier (Stanford Research Systems, Sunnyvale, CA, USA). The current output from the amplifier was recorded using a DAQ board in conjunction with a program written in Labview (National Instruments, Austin, TX, USA). All experiments were conducted at ambient temperatures.

Teflon-coated fused-silica capillaries (100 μm I.D.) were purchased from Polymicro Technologies (Phoenix, AZ, USA). DB-WAX capillaries (100 μm I.D.) for CE experiments were obtained from J & W Scientific (Folsom, CA, USA). Glass chips with a single T-injector design were fabricated in the laboratory. Photomask layout was performed using AutoCAD 2000 (Autodesk, San Rafael, CA, USA) and the generated file was converted to GDS format. The photomask was manufactured by Photo Sciences (Torrance, CA, USA). Schott D263 glass wafers were purchased from S. I. Howard Glass (Worcester, MA, USA). A Cooke (Cooke Vacuum Products, Norwalk, CT, USA) sputtering system was used to deposit the metal etch mask. A Karl Suss (Karl Suss America, Waterbury Center, VA, USA) MA6 contact mask aligner was used for photolithography. The microchannel dimensions were 25 μm deep and 50 μm wide; the separation channel length was 8.0 cm and the injection arms were 1.0 cm each.

2.2. Chemicals

High-purity potassium phosphate, thiourea and acetonitrile were used as received from Aldrich (Milwaukee, WI, USA). Sodium tetraborate was obtained from Sigma (St Louis, MO, USA). Napthalene-2,3-dicarboxaldehyde (NDA) and potassium cyanide were purchased from Molecular Probes (Eugene, OR, USA). All phenylthiohydantoin (PTH) amino acids and peptides were purchased from Sigma. Water was purified with an Ultra-Pure water system from Millipore (Milford, MA, USA). (Acrylamidomethyl)cellulose acetate butyrate was obtained from Aldrich and used as received. Other acrylate monomers were obtained and purified as previously described [24]. OCG 825 photoresist and OCG 934 developer were obtained from Arch (Columbus, OH, USA). Chrome etch was purchased from Microchrome Technologies (San Jose, CA, USA). High purity sulfuric acid and hydrofluoric acid were obtained from Ashland (Norwalk, CT, USA), and acetone and ammonium hydroxide were purchased from General Chemical (Parsippany, NJ).

2.3. Polymer stationary phases

Prior to in situ polymerization, the walls of capillaries and microchannels were silanized to ensure covalent attachment of the polymer to the substrate; this pretreatment has been previously described [24]. Both positively- and negatively-charged porous polymer monoliths containing butyl (C_4) and lauryl (C_{12}) groups were prepared according to a previously described procedure [24]. In the lauryl material, lauryl acrylate replaced 10% of the butyl monomer. The cellulose material was prepared from monomers in the following percentages: 1% (acrylamidomethyl)cellulose acetate butyrate, 10% tetrahydrofurfuryl (THF) acrylate, 1% [2-(acryloyloxy)ethyl]trimethylammonium methylsulfate, 58% butyl acrylate, 30% 1,3-butanediol diacrylate. The glass capillaries were pretreated to ensure adhesion of the polymer monoliths to the wall. For the positive material, a positive pretreatment solution was used to reverse the EOF as well as to promote adhesion.

2.4. CEC experiments

The packed capillary was electrokinetically conditioned using acetonitrile–5 m*M* Tris buffer pH 8 (80:20, v/v) or acetonitrile–25 m*M* phosphate buffer pH 2.8 (80:20, v/v) to remove residual monomeric materials prior to use. A detection window in the polymer was formed by exposure to 214 nm light from a UV light source.

For isocratic CEC separations of PTH-labeled amino acids using UV detection, negatively-charged butyl or lauryl monoliths (functionalized with sulfonic acid groups) were employed as stationary phases. The mobile phase was prepared by mixing the appropriate percentage of acetonitrile (by volume) in 25 m*M* phosphate solution pH 7.3 and was degassed by ultrasonication prior to use. The capillary was conditioned in the running buffer for approximately 1 h. Stock solutions of individual

PTH–amino acids were prepared in water and acetonitrile and sample solutions were diluted appropriately with buffer solution to attain final amino acid concentrations of 10^{-4} to 10^{-3} *M*. Thiourea (2.5 m*M*) was added to each sample mixture as the unretained marker. Amino acid samples were injected electrokinetically at the anode for 5 s at 2 kV and separations were performed at constant field strengths of 150–300 V/cm.

For isocratic CEC separations of native peptides using UV detection, positively-charged butyl monoliths (containing quaternary ammonium moieties) were used as stationary phases. The mobile phase (acetonitrile–12.5 m*M* phosphate buffer pH 2.8; 30:70, v/v) was degassed before use. The packed capillary was conditioned in this running buffer for 1 h. Peptide stock solutions (10^{-3} *M*) were prepared in water and final peptide samples of approximately 10^{-5} *M* were made by diluting with the running buffer. Peptide samples were electrokinetically injected at the cathode for 5 s at 1.5 kV and separated at constant field strengths of 90–200 V/cm.

For isocratic CEC separations of NDA-labeled amino acids using LIF detection, negatively-charged lauryl monoliths (functionalized with sulfonic acid groups) were employed as stationary phases. The mobile phase was prepared by mixing the appropriate percentage of acetonitrile (by volume) in 25 m*M* phosphate solution pH 7.2 and was degassed prior to use. The packed capillary was conditioned in the running buffer for approximately 1 h. Stock solutions of amino acids were prepared in water and working solutions of 0.3 m*M* were prepared by diluting in 50 m*M* borate buffer pH 9.5. Derivatization was carried out by adding aliquots of 40 μl of 4.8 m*M* KCN and 40 μl of 2.4 m*M* NDA to the 0.3 m*M* amino acid solution. The solutions were diluted with the run buffer to obtain final concentrations of 10^{-8} *M*. Amino acid samples were injected electrokinetically at the anode for 2 s at 4 kV and separations were performed at constant field strengths of 200 V/cm.

For on-chip electrochromatographic separations of peptides, negatively-charged lauryl monoliths (containing sulfonic acid groups) were cast in the microchannels. The mobile phase (acetonitrile–12.5 m*M* phosphate buffer pH 7.3; 35:65, v/v) was degassed before use. The packed channels were conditioned in this running buffer for 1 h. The peptides were labeled by adding a 40 μl aliquot of 0.3 m*M* peptide stock solution to 1 ml of 50 m*M* borate buffer pH 9.5, followed by aliquots of 40 μl of 4.8 m*M* KCN and 40 μl of 2.4 m*M* NDA. The solutions were diluted with the run buffer to obtain final concentrations of 10^{-6}– 10^{-7} *M*. Peptide samples were electrokinetically injected at the cathode for 30 s at 1.0 kV and separated at a constant field strength of 1200 V/cm. LIF was employed as the means of detection. An algorithm developed in-house was used for background subtraction and smoothing for all chromatographic data.

2.5. CE experiments

Unpacked, coated DB-WAX capillaries were used in order to eliminate EOF at the inner walls. The mobile phase (acetonitrile–12.5 m*M* phosphate buffer pH 2.8; 30:70, v/v) was degassed before use. Peptide sample solutions of approximately 10^{-5} *M* were hydrodynamically injected at the cathode for 10 s and separated at constant field strengths of 90–200 V/cm.

2.6. Chip fabrication

Glass wafers were sputtered with chrome (200 nm) which served as the etch mask. A 1-μm-thick layer of OCG 825 positive photoresist was spin-coated and soft-baked (90°C, 5 min). After exposure, the photoresist was developed with OCG 934 developer and hard-baked (120°C, 30 min). Exposed chrome was etched with a commercially available chrome etch and the subsequently exposed glass was etched with 25% HF solution. The photoresist was removed with acetone and the chrome mask was etched as described. Holes (1.0 mm diameter) were drilled in glass cover plates. The etched wafers and cover plates were cleaned with H_2SO_4–H_2O_2 (3:1)(90°C) and NH_4OH–H_2O–H_2O_2 (1:5:1)(60°C), aligned for contacting, and once contacted were thermally bonded at 650°C.

3. Results and discussion

3.1. Porous polymer monoliths

Acrylate-based porous polymer monoliths de-

veloped in our laboratory possess several properties that make them well-suited as reversed-phase chromatographic media [24]. They are readily cured (5 min in capillaries, and 10–20 min in microchannels) by UV irradiation and do not require retaining frits since they are covalently attached to the substrate surface. They support EOF as cast without the need to flush with pressure. They can be made from a wide variety of monomers, enabling the charge and hydrophobicity of the stationary phase to be easily tuned. High efficiencies (>150 000 plates/m) have been routinely obtained in the CEC separations of polyaromatic hydrocarbons and neutral aromatics using negatively- and positively-charged materials with varying degrees of hydrophobicity [24]. In this work, the applicability of both negative and positive polymer monoliths in the CEC separation of charged analytes was investigated.

In the negatively-charged material used for amino acid separations, a sulfonic acid monomer is incorporated to support EOF and the linear alkyl acrylates serve as hydrophobic sites for chromatographic retention. Scanning electron miscroscope (SEM) micrographs indicate that the polymer nodule structure is identical in both butyl and lauryl materials [24]. In both monoliths, the peak pore diameter by porosimetry is approximately 1 μm and the surface area by BET analysis is 1–3 m^2/g [24]. Fig. 1a is a representative SEM micrograph of a negative lauryl monolith.

In the positively-charged porous polymer monoliths used for peptide separations, a tetraalkylammonium compound serves as the charged functionality. The polymer nodule structure is similar to that observed for the negatively-charged materials, as shown by SEM microscopy (Fig. 1b), and BET

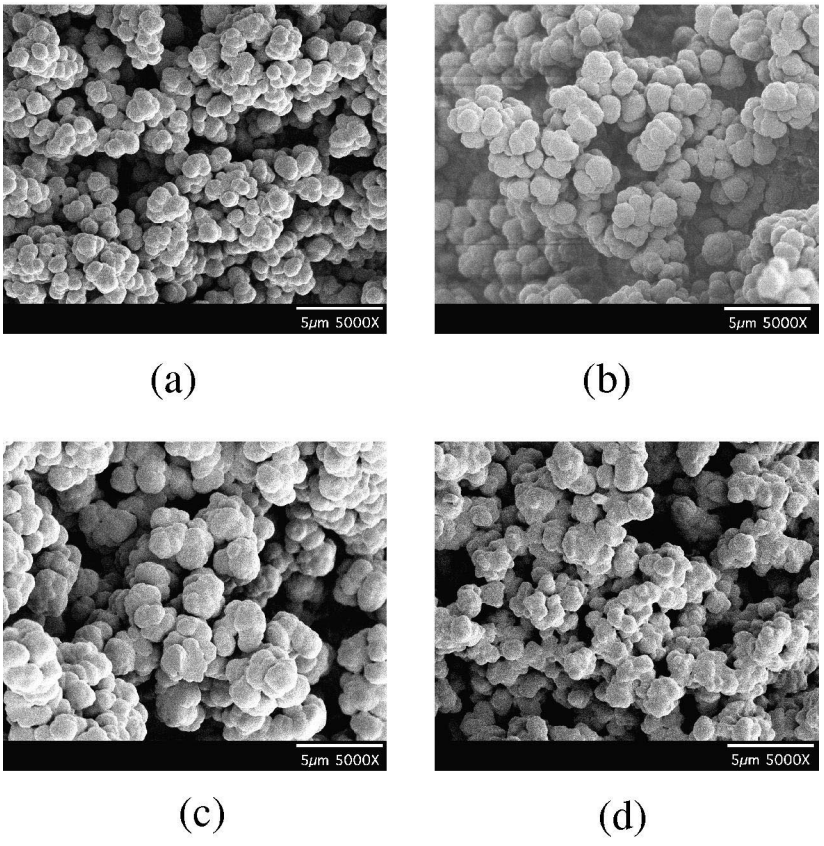

Fig. 1. SEM micrographs of methanol-extracted samples of (a) negatively-charged lauryl monolith, (b) positively-charged butyl monolith, (c) positively-charged butyl monolith with double the percentage (1%) of charged monomer, and (d) positively-charged butyl monolith with 1% cellulose.

surface area is 1–3 m^2/g. Unlike the negative monoliths, however, the positive materials exhibit a range of pore sizes between 1–2 μm without a distinct peak pore diameter (data not shown). In an effort to increase EOF, monoliths with twice the percentage of charged monomer were prepared with no significant effect on the morphology as depicted in Fig. 1c. Incorporation of 1% cellulose to the monomer mixture resulted in slightly smaller polymer nodule sizes (Fig. 1d). This is probably caused by solubility changes when including the more hydrophilic cellulose-based acrylate monomer in the growing monolith network.

3.2. Separation of PTH–amino acids

Peptide sequencing via Edman degradation renders the resultant PTH–amino acids neutral except for PTH–Arg, which is basic, and PTH–Asp and PTH–Glu, which are acidic. PTH–Thr exhibits two peaks, as observed by others [13]. The isocratic CEC separation of 20 PTH–amino acids was achieved using a lauryl (C_{12}) monolithic column containing highly acidic sulfonic acid groups. The mobile phase consisted of acetonitrile–25 m*M* phosphate buffer at pH 7.3; (40:60, v/v). As shown in Fig. 2, neutral hydrophilic amino acids elute first and all in this group but PTH–Gln and PTH–Asn are baseline-resolved. The neutral hydrophobic amino acids are significantly more retained and elute much later, as illustrated by PTH–Phe, PTH–Ile, PTH–Trp and PTH–Leu. PTH–Arg has an electrophoretic mobility in the same direction as EOF, whereas PTH–Asp and PTH–Glu have electrophoretic mobilities that oppose EOF. Since the acidic amino acids elute before PTH–Arg, we may conclude that the separation mechanism under these conditions is dominated by the hydrophobic interactions between the analytes and the monolithic stationary phase rather than by CZE. For the charged amino acids, coulombic interactions will also significantly influence retention. The PTH–Arg peak is broader and more asymmetric because it is also partly retained by electrostatic interactions with the negatively charged sulfonic acid groups of the monolith.

Separation efficiencies of up to 268 000 plates/m are obtained with the lauryl column as shown in Table 1. These values are comparable to those reported for conventional silica-based stationary phases used to separate neutral and acidic PTH–

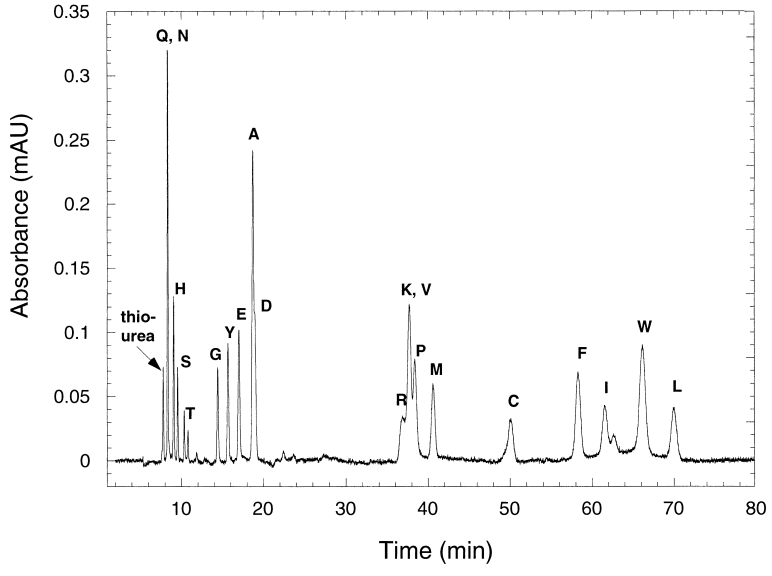

Fig. 2. Electrochromatographic separation of 20 PTH–amino acids on negatively-charged lauryl stationary phase in acetonitrile–25 m*M* phosphate pH 7.3 (40:60, v/v). UV detection at 214 nm. Field strength, 175 V/cm. Capillary: total length = 28.5 cm; length to detector = 17.5 cm; I.D. = 100 μm.

Table 1
Retention times, capacity factors and column efficiencies for the CEC separation of five PTH–amino acids using lauryl and butyl monolithic stationary phases

Amino acid	Lauryl			Butyl		
	t_r (min)	k'	N (plates/m)	t_r (min)	k'	N (plates/m)
PTH–Ala	18.7	1.41	176 000	10.6	1.07	127 000
PTH–Asp	18.9	– [a]	181 000	12.1	– [a]	134 000
PTH–Arg	36.8	– [a]	46 000 [b]	17.5	– [a]	14 000 [b]
PTH–Phe	58.3	6.50	238 000	24.8	3.84	120 000
PTH–Trp	66.2	7.51	268 000	27.0	4.28	116 000

[a] k′ cannot be calculated for charged analytes because retention depends on both chromatographic retention and electrophoretic mobility.
[b] The number of theoretical plates for the asymmetric PTH–Arg peak was obtained using the equation [22]: $N = 41.7\ (t_r/w_{0.1})^2/(A/B + 1.25)$.

amino acids by CEC. Efficiencies in the range of 60 000–213 000 plates/m have been achieved with 3 μm ODS-modified silica particles [13] while values of 176 000–530 000 plates/m have been obtained with 1.5 μm ODS-modified non-porous particles [11]. Mercury porosimetry indicates that the peak pore size of our acrylate-based monoliths is approximately 1 μm [24]. In phase-separated structures such as ours, we often observe a correlation between nodule size and pore size.

3.2.1. Effect of column hydrophobicity

The degree of column hydrophobicity has a significant effect on selectivity and on the quality of separations. Using a representative subset of PTH–amino acids, we compared the separation performance of a negative butyl (C_4) monolithic column to the negative lauryl (C_{12}) material. Under identical mobile phase conditions, column lengths and EOF velocities, we found that including 10% lauryl acrylate in the porous polymer monolith increases the retention times of all amino acids, and the most dramatic increase in capacity factor was observed for the most hydrophobic amino acids, PTH–Phe and PTH–Trp (Table 1). A concomitant increase in efficiencies was also noted and is probably due to differences in the morphologies of the butyl and lauryl materials. Resolution was generally greatly improved and well separated peaks were obtained for the PTH–Gln and PTH–His pair as well as for the group of amino acids consisting of PTH–Gly, PTH–Tyr, PTH–Glu and PTH–Ala, none of which could be baseline-resolved using the less hydrophobic column. However, while the PTH–Ala/PTH–Asp and PTH–Arg/PTH–Lys pairs could not be well-resolved on the lauryl column, they were well separated using the butyl column (data not shown). In addition, the elution order of PTH–Ala and PTH–Glu obtained with the lauryl column is reversed in the butyl stationary phase.

3.2.2. Effect of acetonitrile content

The volume percentage of acetonitrile in the mobile phase was found to dramatically affect the elution order of PTH–amino acids. A subset of amino acids was separated on a negative butyl (C_4) column using different volume ratios of acetonitrile–25 m*M* phosphate pH 7.3. Retention times were normalized with respect to the EOF to give a retention factor t_r/t_{eof}, which depends on both hydrophobic retention as well as electrophoresis (Fig. 3). In reversed-phase chromatography, separation is based on the partition of analytes between the hydrophobic stationary phase and the relatively polar mobile phase, hence increasing mobile phase polarity increases analyte retention. As shown in Fig. 3, the retention times of the neutral amino acids, particularly the most hydrophobic ones, increase as the acetonitrile content in the mobile phase is lowered.

For the charged amino acids, however, the separation mechanism is comprised of an electrophoretic component as well as a chromatographic one. It is possible to alter the balance of these two separation components to achieve the desired resolution and analysis speed by changing the mobile phase com-

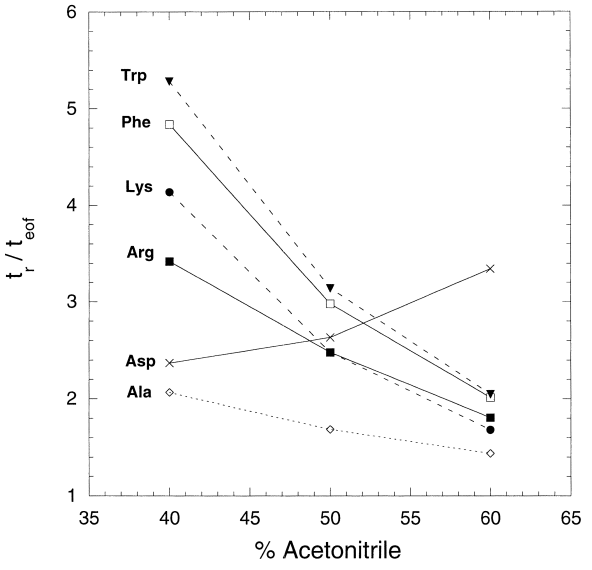

Fig. 3. Plot of normalized retention factor, t_r/t_{eof}, vs. percentage of acetonitrile for five PTH–amino acids separated on a negatively-charged butyl column. Capillary: total length = 25.0 cm; length to detector = 15.2 cm; I.D. = 100 μm.

position. At acetonitrile–25 m*M* phosphate (60:40), PTH–Ala elutes first, followed by PTH–Lys, positively-charged PTH–Arg, neutral hydrophobic PTH–Phe and PTH–Trp, and finally negatively-charged PTH–Asp. This elution order suggests that the amino acid separation is primarily due to the differences in electrophoretic mobility. CZE is still a major component in the separation mechanism at acetonitrile–25 m*M* phosphate buffer (50:50), where PTH–Arg elutes before PTH–Asp, but the degree of retention of the hydrophobic amino acids is significantly increased as indicated by the higher t_r/t_{eof} values. At a ratio of acetonitrile–25 m*M* phosphate (40:60), all the amino acids are significantly more retained except PTH–Asp, which now elutes before PTH–Arg, indicating that chromatographic interactions dominate the separation mechanism.

The acetonitrile content in the mobile phase also influences the EOF velocity, which is 6.81, 6.76, and 5.12 mm/s at 60%, 50% and 40% acetonitrile, respectively. By increasing the percentage of acetonitrile, the electrolyte concentration is concurrently decreased, which results in an increase in the zeta potential and hence a corresponding increase in the EOF velocity [25].

3.3. Separation of NDA-labeled amino acids

Significantly lower limits of detection can be achieved using LIF to detect amino acids derivatized with a fluorogenic reagent. NDA reacts with primary amines in the presence of cyanide to yield highly stable 1-cyano-2-alkylbenz[f]isoindole (CBI) adducts which exhibit high fluorescence quantum yields [26–30]. Upon NDA-labeling, most amino acids possess a single negative charge with the exception of NDA–Glu and NDA–Asp, which possess two negative charges, and NDA–Arg, which is neutral. Labeling difficulties are associated with Lys and Cys due to intramolecular fluorescence quenching [31], and Pro cannot be labeled with NDA because it does not possess a primary amine. Fig. 4 shows the isocratic CEC separation of 15 NDA-labeled amino acids (concentrations of 10^{-8} *M*) employing sensitive LIF detection and using a lauryl (C_{12}) monolith containing sulfonic acid groups and a mobile phase of acetonitrile–20 m*M* phosphate buffer at pH 7.2 (15:85, v/v). NDA–Glu and NDA–Asp could be separated (data not shown) on the same stationary phase using a mobile phase of acetonitrile–12.5 m*M* phosphate buffer at pH 7.2 (15:85, v/v) with retention times of 50.8 min and 58.4 min, respectively (a lower buffer concentration was necessary to achieve faster separations of these two doubly-nega-

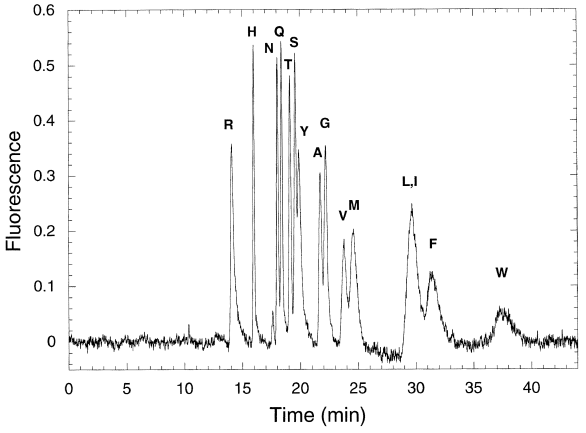

Fig. 4. Electrochromatographic separation of 15 NDA–amino acids on negatively-charged lauryl stationary phase in acetonitrile–20 m*M* phosphate pH 7.2 (15:85, v/v). LIF detection at 413 nm. Field strength, 200 V/cm. Capillary: total length = 33.0 cm; length to detector = 23.5 cm; I.D. = 100 μm.

tive species on the negatively charged stationary phase). Fourteen of the 15 NDA-labeled amino acids are well resolved with only NDA–Leu and NDA–Ile coeluting, and efficiencies in the range of 65 000–371 000 plates/m were obtained. The resolution of our NDA–amino acid separations compare favorably with those achieved using gradient elution HPLC–LIF on C_{18} stationary phases [27,28,30,32], demonstrating the applicability of both CEC and polymer monolithic stationary phases in the separation of charged analytes.

3.4. Separation of basic bioactive peptides

Separation of peptides by CEC requires consideration of the nature of the charged groups on the stationary phase and the pH of the mobile phase. Peptides possess a characteristic isoelectric point (p*I*) and so their net charge varies with the pH of the solution. If the p*I* values of the peptides are known, the pH of the mobile phase should be chosen so as to minimize the electrostatic attraction between most of the peptides and the stationary phase. This can be achieved by careful selection of a stationary phase and a mobile phase pH that will allow the peptides to have the same sign of charge as that of the chromatographic support. However, this leads to the peptides migrating electrophoretically in a direction opposite to the EOF, potentially slowing down their migration. Another factor to consider is the instability of siloxane bonds that link the monolith to the capillary wall at a pH of 8 or higher, thereby requiring separation to be performed at acidic or neutral pH. We selected eight bioactive peptides that had p*I* values ranging from 8.5–8.9 as model analytes for CEC that was performed at a pH of 2.8. This necessitates the use of a monolithic column containing basic groups such as quaternary ammonium in order to suppress electrostatic interactions between the net positively-charged peptides and the charged groups on the stationary phase. Researchers have traditionally obtained positively-charged supports by coating silica particles with silanes functionalized with an amine or quaternary amine but such coatings may be unstable [33] and the EOF is adversely affected by the residual negatively charged silanols [34].

Fig. 5 illustrates the isocratic CEC separation of

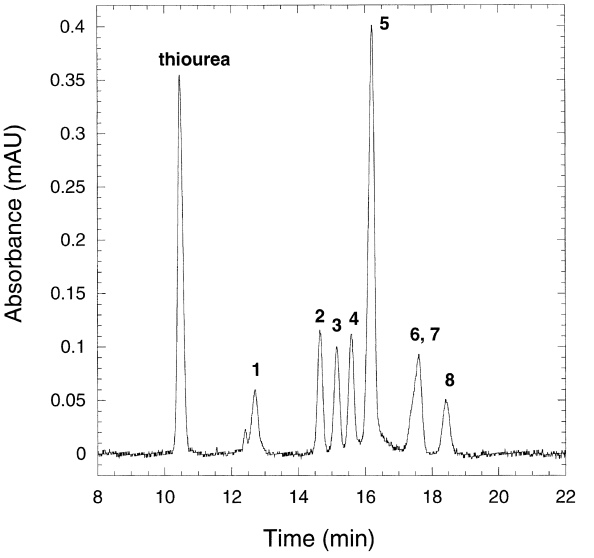

Fig. 5. Electrochromatographic separation of eight bioactive peptides on positively-charged butyl stationary phase incorporated with 0.5% charge in acetonitrile–12.5 m*M* phosphate pH 2.8 (30:70, v/v). UV detection at 214 nm. Field strength, 93 V/cm. Capillary: total length = 32.5 cm; length to detector = 18.5 cm; I.D. = 100 μm. The numbers labeling the peaks correspond to the designations in Table 2.

eight bioactive peptides using a monolithic butyl column containing quaternary ammonium groups (0.5%, w/w) and a mobile phase of acetonitrile–12.5 m*M* phosphate buffer at pH 2.8 (30:70, v/v) . All peptides are baseline resolved except for thymopentin (**6**) and splenopentin (**7**), which differ by only one CH_2 unit (Table 2). Column efficiencies range between 91 000–324 000 plates/m (Table 2), compared to the efficiency value of 43 000 plates/m reported for a peptide separation using a negatively-charged methacrylate-based monolithic stationary phase [8], and values of 32 000–44 000 plates/column, corresponding to 110 000–151 000 plates/m, reported for a CEC separation of four proteins using a positively-charged methacrylate-based monolithic column [7]. Increasing the field strength resulted in a faster EOF velocity and, accordingly, faster peptide elution times.

The peptides were separated by electrophoresis under identical conditions using an open and coated (to eliminate EOF) capillary in order to elucidate the separation mechanism. Only three poorly-resolved peaks were obtained by this method (data not

Table 2
Normalized retention factors and column efficiencies for the CEC separation of eight bioactive peptides using monolithic stationary phases of different compositions

Peptide	Name	Sequence	p*I*	0.5% charge		1% charge		1% charge + 1% cellulose	
				t_r/t_{eof}	*N* (plates/m)	t_r/t_{eof}	*N* (plates/m)	t_r/t_{eof}	*N* (plates/m)
1	Leu–Enkephalin–Lys	YGGFLK	8.59	1.21	92 000	1.25	99 000	1.26	116 000
2	Met–Enkephalin–Arg–Phe	YGGFMRF	8.75	1.40	284 000	1.48	108 000	1.49	213 000
3	α-Casein, fragment 90–95	RYLGYL	8.59	1.45	241 000	1.55	–	1.57	–
4	Met–Enkephalin–Lys	YGGFMK	8.59	1.49	324 000	1.55	–	1.57	–
5	β-Lipotropin, fragment 39–45	KKDSGPY	8.50	1.55	225 000	1.70	138 000	1.69	265 000
6	Thymopentin	RKDVY	8.59	1.68	–	1.87	171 000	1.87	330 000
7	Splenopentin	RKEVY	8.59	1.68	–	1.93	–	1.96	205 000
8	Kyotorphin	YR	8.75	1.76	177 000	1.93	–	1.91	274 000

shown). Leucine–enkephalin–lysine (**1**) and methionine–enkephalin–arginine–phenylalanine (**2**) co-elute to give the first peak, methionine–enkephalin–lysine (**4**) and β-lipotropin (fragment 39–45) (**5**) co-elute as the second peak, and the remaining peptides comprise the third peak.

Retention of peptides in CEC is expected to involve contributions from chromatographic interactions and electrophoretic mobilities of the solutes. In order to elucidate the relative importance of these two contributions, we have used empirical models to calculate retention and migration times for the peptides. A theoretical retention order for small peptides composed of less than 15 amino acid residues may be predicted from a summation of hydrophobicity constants associated with the constituent amino acids for each peptide [35]:

$$t_{Ri} = A \Sigma D_j n_{ij} + B \quad (1)$$

where t_{Ri} is the peptide retention time peptide i, D_j is the retention constant of amino acid j, n_{ij} is the number of amino acid residues j in peptide i, and *A* and *B* are constants determined from data fitting. We used the hydrophobic retention constants calculated by Sasagawa and Teller, which are based on retention times measured on a C_{18} column [35]. Normalization was performed for the retention order so that the least retained peptide corresponds to a retention value of 0 while the most retained peptide corresponds to a retention value of 1. For each retention order, normalization was carried out using (*X* − minimum value)/(maximum value − minimum value), where *X* is the value obtained for peptide X, and minimum and maximum values are the values obtained for the least retained peptide and the most retained peptide, respectively. Fig. 4 clearly shows that the predicted elution order based on this model differs remarkably from what is actually observed, indicating that CZE must play a significant role in the CEC separation.

Furthermore, Fig. 6 illustrates that the elution order follows closely to the order predicted for electrophoretic migration by the ratio $q/M_r^{2/3}$, where

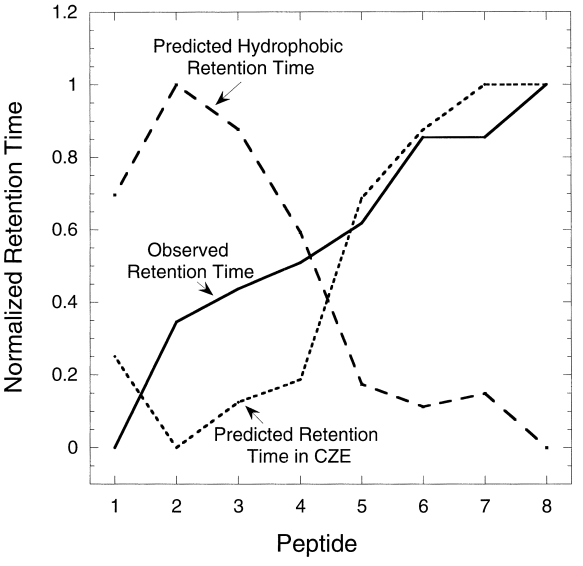

Fig. 6. Plot comparing the observed peptide retention order with the predicted retention orders based on amino acid hydrophobicity constants and calculated electrophoretic factors. The numbers labeling the peptide *x*-axis correspond to the peptide designations in Table 2. The equations used to generate the data are discussed in the text.

q is the net charge of the peptide calculated using the Henderson–Hasselbach equation [36] and adjusted pK_a values for associated amino acids [37], and M_r is the molecular mass [37,38]. The predicted migration order was normalized as described above for the predicted retention order. The correlation between this ratio and electrophoretic mobility has been demonstrated before in the CZE of peptides [37,39,40]. It therefore appears that electrophoretic migration largely determines the peptide elution order but interactions with the stationary phase provide additional selectivity.

The effect of changing stationary phase properties was also investigated. Increasing the surface charge of the monolith resulted in a small increase in the EOF velocity and peptides eluted slightly faster accordingly but with some loss in resolution (Fig. 7). The copolymerization of cellulose ester acrylate, which is used in chiral stationary phases [41,42], improves resolution as shown in Fig. 8. Presumably the incorporation of the polysaccharide to the monolith allows for polar interactions between the cellulose ester and the peptides [42], enabling enhanced resolution of individual peptide peaks. The polymer monoliths can therefore be tuned for selectivity, providing a useful means of separating different sets of peptides. Table 2 compares the normalized retention factors and column efficiencies obtained from the separation of peptides **1**–**8** using the different monolithic stationary phases.

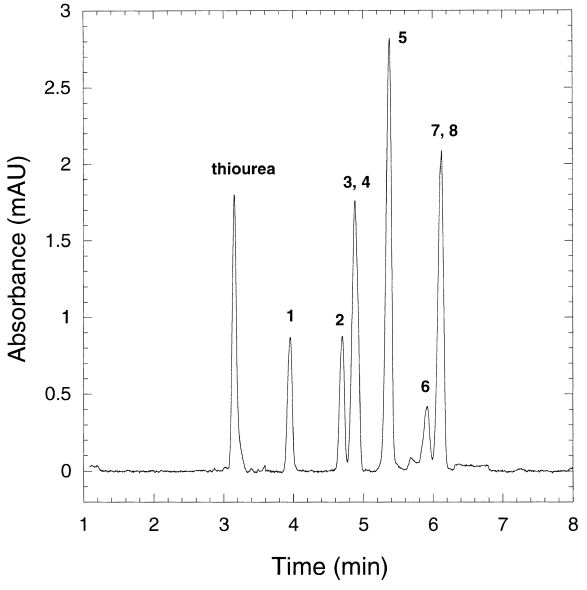

Fig. 7. Electrochromatographic separation of eight bioactive peptides on positively-charged butyl stationary phase incorporated with 1% charge in acetonitrile–12.5 m*M* phosphate pH 2.8 (30:70, v/v). UV detection at 214 nm. Field strength, 200 V/cm. The numbers labeling the peaks correspond to the designations in Table 2.

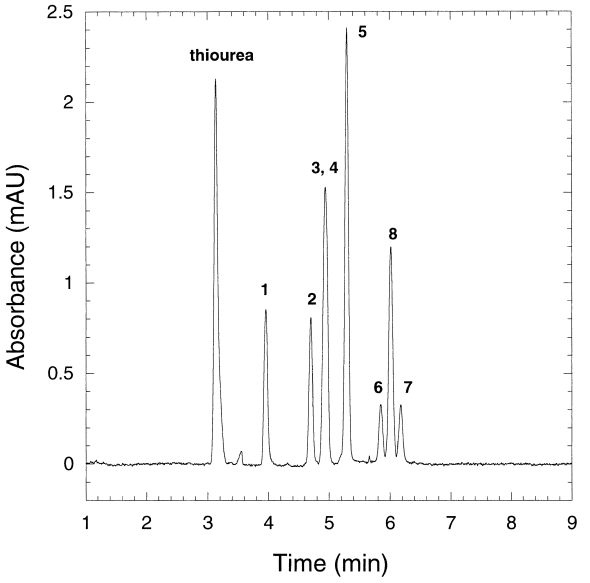

Fig. 8. Electrochromatographic separation of eight bioactive peptides on positively-charged butyl stationary phase incorporated with 1% charge and 1% cellulose ester in acetonitrile–12.5 m*M* phosphate pH 2.8 (30:70, v/v). UV detection at 214 nm. Field strength, 200 V/cm. The numbers labeling the peaks correspond to the designations in Table 2.

3.5. On-chip CEC separation of bioactive peptides

Our porous polymer monoliths were designed for rapid and facile placement in the channels of glass-based microfluidic devices, obviating the need for frits and the difficulties of packing silica beads. Pretreatment of the substrate surface ensures that the polymer is covalently attached to the substrate, and polymerization under UV irradiation is between 10 and 20 min in microchannels. The material supports sufficient EOF as cast and no pressure is required for purging. To demonstrate the applicability of polymer monoliths for chip-based CEC separations, Fig. 9 shows a preliminary on-chip electrochromatographic

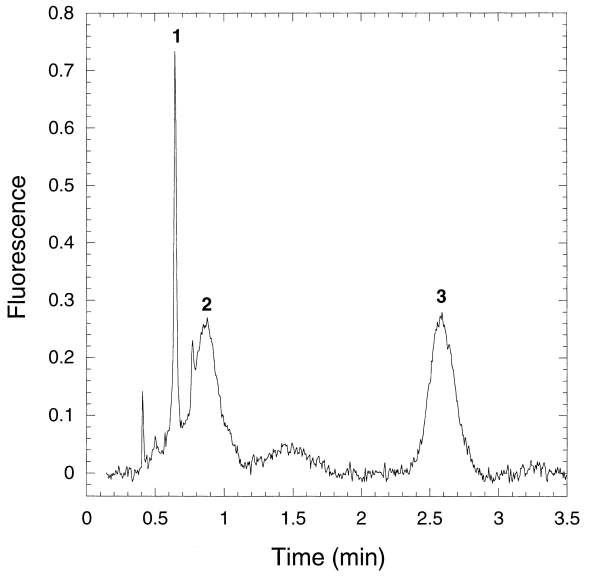

Fig. 9. Electrochromatographic separation of three NDA-labeled bioactive peptides on negatively-charged lauryl monolithic stationary phase cast in a glass chip. LIF detection at 413 nm. Field strength, 1200 V/cm. Mobile phase: acetonitrile–12.5 m*M* phosphate pH 7.0 (35:65, v/v). Microchannel dimensions: 25 μm deep, 50 μm wide; separation channel length, 8.0 cm; injection arms, 1.0 cm each; length to detector, 7.0 cm. Peaks: (1) papain inhibitor, GGYR, (2) α-casein (fragment 90–95), RYLGYL, (3) Ile–angiotensin III, RVYIHPI.

separation of three NDA-labeled bioactive peptides using a monolithic lauryl column containing sulfonic acid groups, a mobile phase of acetonitrile–12.5 m*M* phosphate buffer at pH 7.0 (35:65, v/v), and LIF detection. These peptides contain an arginine residue, which counters the negative charge on the C-terminal carboxyl group that remains after NDA-labeling at a neutral pH. The peptides are baseline-resolved and the column efficiencies are 83 000, 1500 and 11 000 plates/m for papain inhibitor (**1**), α-casein (fragment 90–95) (**2**) and Ile–angiotensin III (**3**), respectively. Although the peptides should be net neutral at this pH, we believe that the broad peaks exhibited by α-casein (fragment 90–95) (**2**) and Ile–angiotensin III (**3**) may be due to electrostatic interactions between the positive charge localized at the N-terminal arginine residue and the negatively-charged stationary phase. In contrast, the positive and negative charges in papain inhibitor (**1**) are both located at the C-terminal arginine residue, allowing more effective charge cancellation.

3.6. Column stability and reproducibility

The monolithic columns were very stable over time and could be used for months without any noticeable degradation in separation efficiency. The single column run-to-run percent standard variation was 2.1% ($n=9$) for the negatively charged lauryl material (based on the retention time for PTH–Glu) and 3.8% ($n=8$) for the positively charged butyl monoliths (based on the retention time for kyotorphin). The column-to-column variation was 10% ($n=3$) and 14% ($n=3$) for the negatively- and positively-charged monoliths, respectively.

4. Conclusions

Acrylate-based porous polymer monoliths have been used as reversed-phase chromatography media for highly efficient and reproducible CEC separations of both neutral and charged PTH–amino acids, NDA-labeled amino acids and bioactive peptides in capillaries and in chips. The monoliths are tunable for charge and hydrophobicity, and incorporation of cellulose esters leads to further changes in selectivity. The separation mechanism of amino acids is strongly influenced by the degree of column hydrophobicity and the mobile phase composition. In CEC of peptides, both electrophoresis and chromatographic retention contribute to speed and selectivity. The present work demonstrates that CEC using porous polymer monolith stationary phases is a powerful technique for separation of charged analytes of biological importance.

Acknowledgements

The authors thank Dr. Issac Shokair for developing the software for data smoothing and background subtraction, George Sartor for help in microfabrication, and Jim Brennan and Gary Hux for technical assistance. This work was supported by the Laboratory Directed Research and Development program of Sandia National Laboratories. Sandia is a multiprog-

ram laboratory operated by Sandia Corporation, a Lockheed Martin Company, for the United States Department of Energy under contract DE-AC04-94AL85000.

References

[1] C.K. Larive, S.M. Lunte, M. Zhong, M.D. Perkins, G.S. Wilson, G. Gokulrangan, T. Williams, F. Afroz, C. Schöneich, T.S. Derrick, C.R. Middaugh, S. Bogdanowich-Knipp, Anal. Chem. 71 (1999) 389R.
[2] K. Stulík, V. Pacáková, J. Suchánková, H.A. Claessens, Anal. Chim. Acta 352 (1997) 1.
[3] J.-T. Wu, P. Huang, M.X. Li, M.G. Qian, D.M. Lubman, Anal. Chem. 69 (1997) 320.
[4] C. Ericson, S. Hjertén, Anal. Chem. 71 (1999) 1621.
[5] A. Apffel, H. Yin, W.S. Hancock, D. McManigill, J. Frenz, S.-L. Wu, J. Chromatogr. A 832 (1999) 149.
[6] J.-T. Wu, P. Huang, M.X. Li, D.M. Lubman, Anal. Chem. 69 (1997) 2908.
[7] S. Zhang, X. Huang, J. Zhang, Cs. Horvath, J. Chromatogr. A 887 (2000) 465.
[8] C. Yu, F. Svec, J.M.J. Fréchet, Electrophoresis 21 (2000) 120.
[9] B. He, J. Ji, F.E. Regnier, J. Chromatogr. A 853 (1999) 257.
[10] G. Choudhary, Cs. Horváth, J.F. Banks, J. Chromatogr. A 828 (1998) 469.
[11] R.M. Seifar, J.C. Kraak, H. Poppe, W.T. Kok, J. Chromatogr. A 832 (1999) 133.
[12] C.G. Huber, G. Choudhary, Cs. Horvath, Anal. Chem. 69 (1997) 4429.
[13] M. Qi, X.-F. Li, C. Stathakis, N.J. Dovichi, J. Chromatogr. A 853 (1999) 131.
[14] C. Ericson, J. Holm, T. Ericson, S. Hjertén, Anal. Chem. 72 (2000) 81.
[15] E.C. Peters, M. Petro, F. Svec, J.M.J. Fréchet, Anal. Chem. 69 (1997) 3646.
[16] E.C. Peters, M. Petro, F. Svec, J.M.J. Fréchet, Anal. Chem. 70 (1998) 2296.
[17] E.C. Peters, M. Petro, F. Svec, J.M.J. Fréchet, Anal. Chem. 70 (1998) 2288.
[18] F. Svec, J.M.J. Fréchet, Anal. Chem. 64 (1992) 820.
[19] F. Svec, J.M.J. Fréchet, Ind. Eng. Chem. Res. 38 (1999) 34.
[20] F. Svec, E.C. Peters, D. Sykora, C. Yu, J.M.J. Fréchet, J. High Resol. Chromatogr. 23 (2000) 3.
[21] A. Palm, M.V. Novotny, Anal. Chem. 69 (1997) 4499.
[22] X. Huang, J. Zhang, Cs. Horváth, J. Chromatogr. A 858 (1999) 91.
[23] I. Gusev, X. Huang, Cs. Horváth, J. Chromatogr. A 855 (1999) 273.
[24] S.M. Ngola, Y. Fintschenko, W.-Y. Choi, T.J. Shepodd, Anal. Chem. 73 (2001) 849.
[25] L.A. Colon, Y. Guo, A. Fermier, Anal. Chem. 69 (1997) 461A.
[26] R.G. Carlson, K. Srinivasachar, R.S. Givens, B.K. Matuszewski, J. Org. Chem. 51 (1986) 3978.
[27] M.C. Roach, M.D. Harmony, Anal. Chem. 59 (1987) 411.
[28] P. de Montigny, J.F. Stobaugh, R.S. Givens, R.G. Carlson, K. Srinivasachar, L.A. Sternson, T. Higuchi, Anal. Chem. 59 (1987) 1096.
[29] B. Matuszewski, R. Givens, K. Srinivasachar, R. Carlson, T. Higuchi, Anal. Chem. 59 (1987) 1102.
[30] F. Lai, T. Sheehan, Biotechniques 14 (1993) 642.
[31] M. Oates, J. Jorgenson, Anal. Chem. 61 (1989) 432.
[32] S.S. Yang, I. Smetena, Chromatographia 37 (1993) 593.
[33] A. Cifuentes, M.A. Rodríguez, F.J. García-Montelongo, J. Chromatogr. A 742 (1996) 257.
[34] D. Corradini, J. Chromatogr. B 699 (1997) 221.
[35] T. Sasagawa, D.C. Teller, in: W.S. Hancock (Ed.), CRC Handbook of HPLC for the Separation of Amino Acids, Peptides, and Proteins, Vol. 2, CRC Press, Boca Raton, FL, 1984, p. 53.
[36] D.C. Harris, Quantitative Chemical Analysis, Freeman, New York, 1999.
[37] E.C. Rickard, M.M. Strohl, R.G. Nielsen, Anal. Biochem. 197 (1991) 197.
[38] S. Fu, C.A. Lucy, Anal. Chem. 70 (1998) 173.
[39] N. Adamson, P.F. Riley, E.C. Reynolds, J. Chromatogr. 646 (1993) 391.
[40] H.G. Lee, D.M. Desiderio, J. Chromatogr. A 666 (1994) 271.
[41] A. Ishikawa, T. Shibata, J. Liq. Chromatogr. 16 (1993) 859.
[42] Y. Okamoto, E. Yashima, Angew. Chem. Int. Ed. Engl. 37 (1998) 1020.

Distribution:

4	MS1425	Carol I. Ashby	1744
3	MS9403	Timothy J. Shepodd	8722
2	MS1425	W. Graham Yelton	1743
2	MS1425	David J. Muron	1744
1	MS0188	LDRD Office	1011
1	MS9018	Central Technical File	8945-1
2	MS0899	Technical Library	9616
1	MS0612	Review & Approval Desk for DOE/OSTI	9612